The homeodomain transcriptional regulator DVE-1 directs a program for synapse elimination during circuit remodeling

The homeodomain transcriptional regulator DVE-1 directs a program for synapse elimination during circuit remodeling

Kellianne D. Alexander[1,2], Shankar Ramachandran[1], Kasturi Biswas[1,2], Christopher M. Lambert[1], Julia Russell[1], Devyn B. Oliver[1,2], William Armstrong[1], Monika Rettler[1], Samuel Liu[1,2], Maria Doitsidou[3], Claire Bénard[1,4], Amy K. Walker[5] Michael M. Francis[1,2*]

[1]Department of Neurobiology, University of Massachusetts Chan Medical School, Worcester, MA

[2]Program in Neuroscience, University of Massachusetts Chan Medical School, Worcester, MA

[3]Centre for discovery brain sciences, University of Edinburgh, Edinburgh, Scotland

[4]Department of Biological Sciences, Université du Québec à Montréal, Quebec, Canada

[5]Program in Molecular Medicine, University of Massachusetts Chan Medical School, Worcester, MA

*Corresponding author: Michael.Francis@umassmed.edu

Abstract

The elimination of synapses during circuit remodeling is critical for brain maturation; however, the molecular mechanisms directing synapse elimination and its timing remain elusive. We show that the transcriptional regulator DVE-1, which shares homology with special AT-rich sequence-binding (SATB) family members previously implicated in human neurodevelopmental disorders, directs the elimination of juvenile synaptic inputs onto remodeling *C. elegans* GABAergic neurons. Juvenile acetylcholine receptor clusters and apposing presynaptic sites are eliminated during the maturation of wild-type GABAergic neurons but persist into adulthood in *dve-1* mutants, producing heightened motor connectivity. DVE-1 localization to GABAergic nuclei is required for synapse elimination, consistent with DVE-1 regulation of transcription. Pathway analysis of putative DVE-1 target genes, proteasome inhibitor, and genetic experiments implicate the ubiquitin-proteasome system in synapse elimination. Together, our findings define a previously unappreciated role for a SATB family member in directing synapse elimination during circuit remodeling, likely through transcriptional regulation of protein degradation processes.

Introduction

The mature human brain is composed of billions of neurons that are organized into functional circuits based on stereotyped patterns of synaptic connections that optimize circuit performance. Mature circuit connectivity is choreographed through a remarkable period of developmental circuit rewiring that is broadly conserved across species [1-4]. During this rewiring or remodeling phase, the mature circuitry is established through a tightly controlled balance: on the one hand, degenerative processes promote the elimination of juvenile synapses, while on the other hand, maintenance or growth processes support the stabilization or formation of new connections. A combination of cell-intrinsic and extrinsic factors shape the progression of these events. For instance, activity-dependent microglial engulfment and elimination of synaptic material shapes connectivity of the retinogeniculate system in mice [5-8], while cell-intrinsic genetic programs such as the circadian clock genes Clock or Bmal1 influence GABAergic maturation and plasticity-related changes in the neocortex [9]. Whereas molecular mechanisms supporting axon guidance and synapse formation have received considerable attention, our understanding of neuron-intrinsic molecular mechanisms controlling synapse elimination remains more limited. In particular, it is unclear how neuron-intrinsic synapse elimination processes are engaged in developing neural circuits. Improved mechanistic knowledge of these processes offers potential for important advances in our grasp of brain development. This knowledge may also inform the pathology underlying numerous neurodevelopmental diseases associated with altered connectivity and neurodegenerative diseases where synapse loss is a hallmark feature. Indeed, recent work has suggested intriguing parallels between the elimination of synapses during development and neurodegenerative processes during disease [10-13].

The nematode *Caenorhabditis elegans* offers significant assets for addressing mechanistic questions about developmental neural circuit remodeling, particularly synapse elimination. *C. elegans* progresses through a highly stereotyped period of nervous system remodeling that establishes the neural connections characteristic of mature animals. 80 of the 302 neurons composing the adult nervous system, including 52 motor neurons, are born post-embryonically and integrated into pre-existing juvenile circuits following the first larval (L1) stage of development [14, 15]. The incorporation of these post-embryonic born motor neurons is accomplished through a remarkable reorganization of circuit connectivity. One of the most striking aspects of this reorganization is the remodeling of synaptic connections in the GABAergic dorsal D-class (DD) motor neurons (**Figure 1A**) [16, 17]. Immediately after hatch, juvenile cholinergic synaptic inputs onto GABAergic DD neurons are located dorsally, and juvenile DD synaptic outputs onto muscles are located ventrally. During remodeling, the juvenile dorsal cholinergic synaptic inputs onto DD neurons are eliminated, and new synaptic inputs from post-embryonic-born presynaptic cholinergic neurons are established ventrally. In parallel, ventral DD GABAergic synaptic terminals are relocated dorsally, forming new GABAergic synaptic contacts onto dorsal muscles [18-22]. Though we now have a growing appreciation of the cellular processes that direct the post-embryonic redistribution of DD GABAergic outputs onto dorsal muscles, we have a limited understanding of how cholinergic inputs onto DD neurons are remodeled. Prior work suggested a mechanism for antagonizing the remodeling of cholinergic inputs onto DD neurons through temporally controlled expression of the Ig domain family member OIG-1 [23, 24]; however, the mechanisms that promote remodeling of these inputs, in particular their elimination, have remained uncharacterized.

We report the identification of a mechanism for neuron-intrinsic transcriptional control of synapse elimination during remodeling of the *C. elegans* motor circuit. From a forward genetic screen to isolate mutants whose juvenile postsynaptic sites remain present on mature GABAergic DD

neurons, we obtained a mutation in the homeodomain transcriptional regulator *dve-1* that shares homology with mammalian special AT-rich sequence-binding (SATB) family members, which are implicated in human neurodevelopmental disorders such as SATB2-associated syndrome [25, 26]. We show that DVE-1 acts cell autonomously in GABAergic DD neurons to promote the removal of juvenile cholinergic synaptic inputs. Juvenile synaptic inputs are maintained into adulthood in *dve-1* mutants, leading to an accumulation of presynaptic cholinergic material and accompanying effects on circuit function and movement. We further show that precocious synapse elimination in *oig-1* mutants is reversed by mutation of *dve-1*, suggesting that DVE-1 promotes pro-degenerative processes which are antagonized by OIG-1. Our results reveal a neuron-intrinsic mechanism for the regulation of neurodevelopmental synapse elimination through the actions of a conserved homeodomain transcriptional regulator.

Results

Distinct mechanisms direct developmental remodeling of presynaptic terminals versus postsynaptic sites in GABAergic neurons

Previous work by our lab showed that clusters of postsynaptic ionotropic acetylcholine receptors (iAChR) denote postsynaptic sites on DD neurons [23, 27, 28]. These postsynaptic sites undergo dorsoventral remodeling during the transition between the 1st and 2nd larval stages of *C. elegans* development (L1/L2 transition) [23, 24]. During this period, dorsal postsynaptic sites on DD neurons are removed, and new ventral postsynaptic sites are formed as indicated by the appearance of new ventral iAChR clusters (**Figure 1A**). The dorsoventral remodeling of cholinergic postsynaptic sites in DD neurons occurs coincidently with the ventrodorsal rearrangement of GABAergic presynaptic terminals (labeled by the synaptic vesicle marker mCherry::RAB-3) (**Figure 1A; S1.1A,B**). Notably, we found that mutations in several genes previously implicated in the remodeling of GABAergic presynaptic terminals had no appreciable effect on the remodeling of cholinergic postsynaptic sites in DD neurons (**Figure S1.1C, Table 1**). For example, juvenile cholinergic postsynaptic sites are properly removed from the dorsal processes of DD neurons in *ced-3/*caspase mutants (**Figure S1.1C**), while juvenile RAB-3 clusters persist in the ventral nerve cord until much later in development (through the L4 stage) [29]. Indeed, lingering synaptic vesicle clusters in the ventral nerve cord of *ced-3* mutants are interleaved with newly formed ventral iAChR clusters at L4 stage (**Figure S1.1C**), demonstrating that the formation of new ventral postsynaptic sites during remodeling also occurs independently of *ced-3*. Mutations in several genes important for neurotransmitter release and calcium signaling also do not appreciably alter the remodeling of postsynaptic sites in DD neurons, though we noted clear delays in the remodeling of DD presynaptic terminals as found previously [19, 21] (**Table 2**). Of the genes we tested, only mutation of the RyR/*unc-68* gene produced a modest delay in the remodeling of postsynaptic sites, suggesting calcium release from intracellular stores contributes

(**Table 2**). Taken together, our findings demonstrate that mechanisms for remodeling postsynaptic sites in DD neurons are distinct from those previously implicated in the remodeling of DD GABAergic presynaptic terminals.

Identification of *dve-1* as a transcriptional regulator of synapse elimination

Motivated by these findings, we performed a forward mutagenesis screen to identify previously undefined mechanisms controlling the removal of juvenile postsynaptic sites in DD neurons (**Figure S1.2A,B**). From this screen we isolated a recessive mutant, *uf171,* where juvenile postsynaptic sites, indicated by dorsally positioned iAChR clusters, are not properly eliminated during remodeling. Dorsal postsynaptic sites are normally eliminated before the L2 stage (22 hours after hatch) in wild type but remain visible through the late L4 stage (>40 hours after hatch) in *uf171* mutants (**Figure 1B**). Whole genome sequence analysis of *uf171* mutants revealed a point mutation that produces a proline to serine (P/S) substitution in the gene encoding the homeodomain protein DVE-1 (**Figure 1C**). Expression of the wild-type *dve-1* cDNA in *dve-1(uf171)* mutants using either the native promoter region or a GABA-specific promoter restored the normal elimination of juvenile postsynaptic sites (**Figure 1D,E; Figure S1.2C**), while *dve-1* overexpression in wild-type animals did not produce appreciable changes in removal (**Figure 1D; Figure S1.2C,D**). A similar failure in the elimination of juvenile postsynaptic sites is also evident using another available *dve-1* mutant, *dve-1(tm4803)*, that harbors a small insertion/deletion mutation (**Figure 1C,E; Figure S1.2C,D**). The P/S substitution encoded by *dve-1(uf171)* affects a highly conserved proline residue predicted to lie within a loop between helices I and II of the first homeodomain of DVE-1. *dve-1(tm4803)* deletes a portion of predicted helix III in the same homeodomain and a splice site, leading to a 65 bp insertion (**Figure 1C**) [30]. As *dve-1* null mutants are embryonic lethal [31], both mutations are predicted to be hypomorphic. Our

identification of *dve-1* and further analysis demonstrate a cell-autonomous requirement for *dve-1* in DD GABAergic neurons for the neurodevelopmental elimination of juvenile postsynaptic receptors during remodeling. *dve-1* was of particular interest because it encodes a homeodomain transcriptional regulator sharing homology with mammalian SATB transcription factors that have roles in vertebrate neurodevelopment [25, 26]**.** In *C. elegans*, the sole previously characterized function for *dve-1* is in the regulation of a mitochondrial stress response [31].

To better define the requirement for DVE-1 in synapse elimination we next used the AID (auxin inducible degron) system for spatiotemporally controlled DVE-1 degradation (**Figure 2A-F**). In this system, a plant F-box protein, TIR1, mediates auxin-dependent degradation of AID-tagged proteins [32, 33]. We used an engineered *dve-1::AID::wrmScarlet* allele in combination with pan-neuronally expressed *TIR1::BFP::AID* to control DVE-1 degradation (**Figure 2A**). Consistent with prior *dve-1* expression analysis [34]**,** under control conditions *dve-1::AID::wrmScarlet* is expressed in the nuclei of both intestinal cells and ventral cord neurons–solely in the DD neuron nuclei in the ventral nerve cord at L1 stage, and in both VD and DD nuclei at L4 stage (**Figure 2C,D**). The remodeling of postsynaptic iAChR clusters proceeds normally in these animals in the absence of auxin (**Figure 2E,F**). Continuous auxin treatment for ~50 hrs from hatch strikingly decreased both *TIR1::BFP::AID* and *DVE-1::AID::wrmScarlet* levels in neurons. Intestinal *DVE-1::AID::wrmScarlet* was not significantly affected (**Figure 2C,D**), demonstrating that degradation was specific to TIR1 expressing cells. Continuous treatment with auxin for either 50 or 24 hrs after hatch severely disrupted synapse elimination in these animals (**Figure 2E,F**). In contrast, auxin treatment after the completion of remodeling (beginning ~24 hrs after hatch) did not impact the dorsoventral distribution of receptor clusters (**Figure 2E**). Our findings indicate that neuronal DVE-1 is required prior to and/or during the remodeling period for synapse elimination to proceed but DVE-1 is not required later in development to maintain the mature organization of postsynaptic receptors in the circuit.

The postsynaptic scaffold protein LEV-10 is associated with cholinergic postsynaptic sites in body wall muscles and GABAergic neurons [35, 36]. Using a previously characterized *lev-10* allele that enables cell-specific endogenous labeling with split-GFP [36], we investigated the removal of LEV-10 during remodeling (**Figure 2G**). At L1 stage, LEV-10 is primarily associated with dorsal DD processes in wild type and is then redistributed to ventral processes during remodeling. Similar to juvenile iAChR clusters, dorsal LEV-10 scaffolds in GABAergic neurons of *dve-1* mutants are not properly eliminated during remodeling, demonstrating that DVE-1 coordinates the removal of both juvenile postsynaptic receptors and associated proteins. Interestingly, mutation of *dve-1* does not significantly affect ventral postsynaptic sites on DD neurons that are formed during remodeling (**Figure 2H; Figure S2.1A**). Likewise, mutation of *dve-1* has little effect on the density of DD dendritic spines that are formed at the end of remodeling (**Figure S2.1B**) [27, 37, 38]. Thus, DVE-1 governs the elimination of juvenile postsynaptic sites during remodeling without affecting the formation or maturation of new postsynaptic sites. Notably, the remodeling of DD GABAergic presynaptic terminals also occurs normally in *dve-1* mutants (**Figure 2H, Figure S2.1C**), further indicating that distinct neuron-intrinsic programs direct remodeling of the pre- and postsynaptic domains of GABAergic DD neurons.

Lingering iAChRs in *dve-1* mutants are organized into structural synapses

To test if lingering juvenile postsynaptic sites in the dorsal nerve cord of *dve-1* mutants are organized into structurally intact synapses, we first asked whether these iAChR clusters are localized at the cell surface. We found that lingering dorsal iAChR clusters in *dve-1* mutants could be labeled by *in vivo* injection of antibodies to an engineered extracellular HA epitope [38, 39], suggesting localization at the cell surface (**Figure 3A**). We also found that most of the iAChR clusters retained in dorsal GABAergic DD processes of *dve-1* mutants are in close apposition with

synaptic vesicle assemblies and active zones in cholinergic axons of the dorsal nerve cord, suggesting incorporation into structural synapses (**Figure 3B-D**).

During remodeling, cholinergic DA/B connections with DD neurons in the dorsal nerve cord are removed, and new DA/B connections are established with post-embryonic born ventrally directed GABAergic D-class (VD) motor neurons (**Figure 3E**). To investigate how cholinergic presynaptic terminals may be affected by mutation of *dve-1*, we expressed the photoconvertible synaptic vesicle marker Dendra2::RAB-3 in cholinergic DA/B neurons (**Figure 3F-J; Figure S3.1A-G**). We first examined the distribution of Dendra2::RAB-3 in the wild-type dorsal nerve cord immediately prior to the onset of DD remodeling (approximately 14 hours after hatch). Prior to photoconversion, clusters of green Dendra2::RAB-3 fluorescence were distributed along the length of cholinergic axons in the dorsal nerve cord (**Figure S3.1A**). Brief exposure to 405 nm light produced immediate and irreversible photoconversion of Dendra2::RAB-3 from green to red fluorescence (**Figures 3G-J and S3.1B-G**). In wild type, Dendra2::RAB-3 clusters that had been photoconverted to red fluorescence prior to the onset of remodeling were strikingly reduced following remodeling (10 hours later, 55 ± 9% reduction) and were replaced by new synaptic vesicle clusters (green fluorescence) (**Figure 3G,H; Figure S3.1B-D**). In contrast, wild type Dendra2::RAB-3 clusters photoconverted after the completion of remodeling (at approximately 24 hours after hatch) remained largely stable over the subsequent 10 hours (**Figure 3I,J; Figure S3.1E-G**). New green RAB-3 clusters also became visible during this time frame (24-34 hours after hatch), indicating a parallel addition of new vesicular material (**Figure 3I,J; Figure S3.1F,G**). Thus, synaptic vesicle clusters in wild-type DA/B axons are largely removed and replaced during the 10-hour period of remodeling but are more stable over a 10-hour time window immediately following completion of remodeling, offering intriguing evidence for developmental stage-specific regulation of cholinergic synaptic vesicle stability.

We noted a striking change in the stability of synaptic vesicle material in cholinergic axons of *dve-1* mutants during remodeling. Most dorsal cholinergic Dendra2::RAB-3 clusters photoconverted prior to the onset of synaptic remodeling were preserved throughout remodeling in *dve-1* mutants (**Figure 3G,H; Figure S3.1B-D**), indicating enhanced stability of cholinergic terminals presynaptic to DD neurons. The addition of new synaptic vesicles during this time frame (14-24 hours after hatch) was not appreciably affected by mutation of *dve-1*, as indicated by similar increases in green Dendra2::RAB-3 fluorescence across wild-type and *dve-1* mutant cholinergic axons (**Figure 3G,H; Figure S3.1C,D**). RAB-3 clusters that were photoconverted after the completion of remodeling (approximately 24 hours after hatch) remained detectable 10 hours later in *dve-1* mutants, also similar to wild type (**Figure 3I,J; Figure S3.1E-G**). Green Dendra2::RAB-3 fluorescence in dorsal axons increased by roughly 2-fold in *dve-1* mutants compared to wild type at 34 hours after hatch, suggesting enhanced addition or stabilization of new synaptic vesicles at *dve-1* mutant cholinergic axon terminals over the 10 hrs following remodeling (**Figure 3I,J; Figure S3.1F,G**). Consistent with this observation, we noted that the intensity of the synaptic vesicle marker SNB-1::GFP was increased in dorsal cholinergic axons of L4 stage *dve-1* mutants compared to wild type (**Figure 3K**), whereas SNB-1::GFP fluorescence intensity in ventral cholinergic axons of *dve-1* mutants was unchanged (**Figure 3L**). We made a similar observation for the mCherry::RAB-3 synaptic vesicle marker (**Figure S3.1H**). Since the DA/B cholinergic neurons form dyadic synapses with both GABA neurons and muscles as postsynaptic targets, we also examined the apposition of cholinergic SVs with AChRs located in postsynaptic muscle cells and found no appreciable difference with wild type (**Figure S3.1I**). Notably, the fluorescence intensity of active zone markers UNC-10::GFP and ELKS-1::GFP in dorsal cholinergic axons was also not appreciably altered in L4 stage *dve-1* mutants (**Figure S3.1J,K**). Thus, mutation of *dve-1* leads to an increase in the stability or recruitment of synaptic vesicle material at dorsal cholinergic axon terminals but does not appreciably alter the size or density of active zones. Together with our previous findings, these data suggest that DVE-1 promotes destabilization of

both vesicle assemblies in presynaptic cholinergic axons and cholinergic postsynaptic sites in GABAergic neurons during wild-type remodeling.

A failure to eliminate postsynaptic sites leads to enhanced activity and altered motor behavior

We next sought to investigate how a failure of synapse elimination may impact circuit function. We first asked whether the preserved structural connections between dorsal cholinergic axons and GABAergic DD neurons of *dve-1* mutants were functional in adults. To address this question, we used combined cell-specific expression of Chrimson for cholinergic depolarization [40, 41] and GCaMP6 for monitoring [Ca^{2+}] changes in the postsynaptic GABAergic motor neurons [42] (**Figure S4.1A**). We recorded Ca^{2+} transients from young adult GABAergic DD or VD motor neurons in response to presynaptic DA/B cholinergic depolarization. We found that cholinergic photostimulation elicited a modest Ca^{2+} response in roughly 37% of wild-type DD neurons tested, consistent with a low degree of synaptic connectivity between these neurons in adults as predicted by the wiring diagram [15, 43]. The percentage of responsive DD neurons (85%) and the average magnitude of stimulus-elicited Ca^{2+} transients were significantly greater in *dve-1* mutants (**Figure 4A**), demonstrating enhanced functional connectivity between dorsal cholinergic neurons and GABAergic DD neurons of adult *dve-1* mutants.

We next asked how altered functional connectivity in the motor circuit of *dve-1(uf171)* mutants might affect locomotory behavior. Automated tracking of single worms during exploratory behavior showed *dve-1(uf171)* mutants frequently move in loose, dorsally directed circles, whereas wild-type animals are more likely to adopt straight trajectories (**Figure 4B**). During 5 minutes of continuous tracking, roughly 80% of *dve-1(uf171)* mutants circled or curved, approximately 60% of these in the dorsal direction, while only 20% of wild type circled (**Figure 4B,C**). The dorsal

circling behavior of *dve-1* mutants suggested that altered synaptic output from the motor circuit may produce a turning bias. Mature, wild-type dorsally directed DA/B cholinergic motor neurons form dyadic synapses with dorsal body wall muscles and VD GABAergic dendrites. Based on our mutant analysis, we predict that mature DA/B neurons of *dve-1* mutants preserve additional ectopic dorsal connections with DD GABAergic dendrites, leading to increased cholinergic SV material in the cholinergic DA/B axons. We speculated that the increased abundance of cholinergic synaptic vesicles in dorsal motor axons of *dve-1* mutants may enhance cholinergic activation of dorsal muscles and elicit more robust dorsal turning. In support of this idea, we found that *dve-1* mutants were hypersensitive to the paralyzing effects of the acetylcholinesterase inhibitor aldicarb, an indicator of elevated acetylcholine release [44] (**Figure S4.1B**).

To explore this further, we tracked animals during depolarization of dorsal cholinergic neurons by cell-specific photoactivation using Chrimson. Prior to stimulation, control animals moved in predominantly forward trajectories (**Figure 4D**). As expected, photostimulation of DA/B motor neurons (625 nm, 14 mW/cm^2) enhanced dorsal turning in control animals, often leading to large dorsally oriented circles (**Figure 4D,G**). DA/B motor neuron photostimulation elicited heightened turning responses in *dve-1* mutants, increasing dorsal turns by ~2.5 fold compared with photostimulation of controls and leading to tight dorsally oriented circles (**Figure 4D-H**). The enhanced dorsal turning of *dve-1* mutants was associated with an increase in the depth of dorsal bends compared to wild type (**Figure 4G,H, Figure S4.1C,D**) and was not observed in the absence of the chromophore retinal (**Figure S4.1E,F**). Chrimson expression was also not appreciably different across *dve-1* mutants and controls (**Figure S4.1G**). As DA/B cholinergic motor neurons are presynaptic to both GABAergic neurons and dorsal body wall muscles, we propose that increased acetylcholine release enhances dorsal muscle bending and circling in *dve-1* mutants, perhaps due to an increase in the size of the synaptic vesicle pool in dorsal cholinergic axons. Ectopic activation of dorsally projecting GABAergic DD neurons in *dve-1* mutants might

be expected to enhance dorsal inhibition, countering the effects of dorsal excitation. However, the number and strength of synaptic connections from dorsal cholinergic motor neurons to dorsal body wall muscles may overwhelm any increase in dorsal inhibition. Together, our results suggest mutation of *dve-1* impacts functional connectivity both through retention of juvenile connectivity onto DD motor neurons and through an increase in cholinergic transmission onto dorsal muscles. However, we note that alternative models are also possible, such as decreased release from GABAergic DD presynaptic terminals of *dve-1* mutants.

Synapse elimination occurs through a convergence of DVE-1 regulated destabilization and removal of OIG-1 antagonism

The timing of DD neuron remodeling is, in part, determined through temporally controlled expression of the Ig-domain protein OIG-1. Expression of the transcriptional reporter *oig-1pr::*GFP in L1 stage DD neurons is not appreciably changed in *dve-1* mutants (**Figure 5A**), in alignment with prior evidence that other pathways control *oig-1* expression [23, 24]. Likewise, *oig-1* deletion does not appreciably alter DVE-1::GFP expression (**Figure 5A**). OIG-1 is an Ig domain protein that normally antagonizes synaptic remodeling. In *oig-1* mutants, the remodeling of postsynaptic sites in DD neurons occurs precociously compared with wild type, including both the elimination of dorsal juvenile postsynaptic sites and the formation of new ventral postsynaptic sites [23, 24]. While juvenile dorsal postsynaptic sites are removed precociously in *oig-1* single mutants, they are preserved in *oig-1*;*dve-1* double mutants through late L4 stage, similar to *dve-1* single mutants (**Figure 5B-C,F**). DVE-1 is therefore required for synapse elimination in both wild type and *oig-1* mutants where antagonistic processes promoting synapse stabilization are disrupted. Conversely, new ventral postsynaptic sites are formed precociously in both *oig-1* single mutants and *oig-1*;*dve-1* double mutants (**Figure 5D-F**). Thus, disruption of *dve-1* function reverses

precocious synapse elimination in *oig-1* mutants but does not impact the premature assembly of ventral postsynaptic sites, supporting the independence of programs for synapse elimination versus growth, and suggesting independent functions for OIG-1 in each (**Figure 5F**). Overall, our findings show that mature connectivity is sculpted through a convergence of DVE-1 regulated elimination processes and temporally regulated OIG-1 based stabilization mechanisms.

Nuclear localization of DVE-1 in GABAergic neurons is required for synapse elimination

We next used an engineered *dve-1::gfp* allele [45] to investigate potential mechanisms for DVE-1 spatial regulation in GABAergic neurons. As was observed for the *dve-1::AID::wrmScarlet* allele described above, we noted strong DVE-1::GFP expression in intestinal cells, and in roughly 20 neurons at the L1 stage including DD GABAergic neurons (**Figure 6A-C; Figure S6.1 A**). Notably, DVE-1::GFP was specifically localized to DD GABAergic nuclei at L1 stage, where it assembled in discrete nuclear foci during the time frame of synaptic remodeling. Similar nuclear DVE-1 clusters were noted previously in intestinal cell nuclei where DVE-1 is thought to regulate gene expression during the mitochondrial unfolded protein response (mtUPR) by associating with loose regions of chromatin and organizing chromatin loops [45]. We found that DVE-1::GFP expression in GABAergic neurons required the Pitx family homeodomain transcription factor UNC-30, the terminal selector of *C. elegans* GABAergic motor neuron identity (**Figure S6.1B,C**) [46-48]. Mutation of *unc-30* did not appreciably change DVE-1::GFP fluorescence in intestinal cells (**Figure S6.1D**), suggesting cell type-specific mechanisms for *dve-1* expression mediated at least in part through UNC-30 regulation. In support of this idea, mutation of putative UNC-30 binding sites [46-48] identified in the *dve-1* promoter region strikingly reduced *dve-1* expression in GABAergic neurons but had no effect on intestinal *dve-1* expression (**Figure S6.1E**).

Prior studies of DVE-1 in intestinal cells showed that deSUMOylation of DVE-1, mediated by the isopeptidase ULP-4, is required for its nuclear localization [49]. We asked if ULP-4 is similarly required for DVE-1 nuclear localization and synapse elimination in DD GABAergic neurons. Mutation of *ulp-4* caused a striking decrease of nuclear *dve-1::*GFP fluorescence in GABAergic neurons and severely diminished *dve-1::*GFP nuclear foci (**Figure 6B,C**). A mutated form of DVE-1::GFP, DVE-1K327R, where a key lysine residue required for SUMOylation is mutated to arginine [49], localizes to GABAergic nuclei in the absence of *ulp-4* (**Figure 6B,C**). ULP-4 was also required for the elimination of dorsal iAChR clusters during remodeling, such that dorsal iAChR clusters remained present in roughly 50% of L4 stage *ulp-4* mutants (**Figure 6D-F**). Either pan-neuronal or GABA neuron-specific expression of the wild-type *ulp-4* gene in *ulp-4* mutants was sufficient to restore the elimination of dorsal iAChRs, while intestinal *ulp-4* expression was not (**Figure 6D-F**). Further, mutation of the DVE-1 SUMOylation site (K327R) by itself did not impair synapse elimination but restored proper removal of iAChRs in *ulp-4* mutants (**Figure 6D-F**). We conclude that the localization of DVE-1 to GABAergic nuclei is essential for synapse elimination during remodeling, and this localization is regulated at least in part by ULP-4 and SUMOylation. Notably, the nuclear localization of mammalian SATB family members is also dependent on SUMOylation, suggesting conserved regulatory mechanisms [50, 51].

Analysis of potential DVE-1 transcriptional targets reveals several pathways with relevance for synapse elimination

Recent work revealed that homeodomain transcription factors are broadly utilized in the specification of *C. elegans* neuronal identity [34]. Given this finding and DVE-1 homology with mammalian SATB family transcription factors, we asked whether DVE-1 transcriptional regulation may be important for GABAergic neuronal identity. We found that the numbers of DD neurons

and commissures were unchanged in *dve-1* mutants compared to wild type (**Figure S6.2A**). In addition, we found that the expression levels for *oig-1* (**Figure 5A**) and three additional GABAergic markers in DD neurons (*unc-47*/GABA vesicular transporter, *unc-25*/glutamic acid decarboxylase, and *flp-13*/FMRFamide neuropeptide) were not appreciably altered by *dve-1* mutation (**Figure S6.2B**). These results support that DVE-1 is not critical for GABAergic identity of the DD neurons but instead regulates other aspects of GABAergic neuron development.

To reveal potential direct targets of DVE-1 in GABAergic neurons, we analyzed chromatin immunoprecipitation followed by sequencing (ChIP-Seq) data available from the modENCODE consortium [52]. We found 1044 genes with strong DVE-1 binding signal in their promoter regions, implicating these genes as potential direct targets for DVE-1 transcriptional regulation (**File S5**), though we note that overexpression of DVE-1::GFP in the strain used for these experiments could potentially impact this analysis. Through *de novo* motif discovery analysis, we identified four sequences overrepresented in the DVE-1 binding peaks, two of which were identified previously (**Figure S7.1A**)[53]. 627 of the identified potential DVE-1 targets are significantly expressed in GABAergic neurons based on available single-cell RNA-seq data (**File S5**) [54, 55]. Pathway analysis of the GABAergic neuron-enriched targets using WormCat [56] and WormenrichR [57] revealed a significant enrichment of genes involved in the mitochondrial unfolded protein response (mtUPR) stress pathway (**Figure 7A, Figure S7.1B, File S5)**, as expected from prior studies [31, 49, 58]. Notably, our analysis also revealed enrichment of genes involved in the ubiquitin-proteasome system (UPS), as well as various other processes including ribosomal composition, and endocytic and phagocytotic function (**Figure 7A, Figure S7.1B, Supplementary Table 1, File S5**) that represent intriguing potential targets for DVE-1 regulation of synapse elimination.

Inhibition of the ubiquitin-proteasome system, but not activation or inhibition of the mtUPR, delays DVE-1-dependent synapse elimination

To assess which of the pathways identified from our analysis may be most critical, we next asked whether DVE-1 regulates synapse elimination by activating or inhibiting the mtUPR. We first quantified the length and density of mitochondria in DD neurons and found no differences between wild type and *dve-1* mutants (**Figure S7.2A**). We next measured mtUPR activation in *dve-1* mutants by quantifying the fluorescence of *hsp-6pr::*GFP, a commonly used mtUPR reporter [31]. Surprisingly, we noted increased levels of intestinal *hsp-6pr::*GFP expression in *dve-1* mutants compared with control, suggesting elevated mtUPR activity (**Figure S7.2B,C**). The transcription factor ATFS-1 is required for the *hsp-6pr::*GFP transcriptional response and activation of the mtUPR [59]. RNAi knockdown of *atfs-1* decreased *hsp-6pr::*GFP expression in *dve-1* mutants (**Figure S7.2C**), indicating that downregulation of *atfs-1* reduced mtUPR activation. However, inhibition of the mtUPR by *atfs-1* knockdown failed to restore normal removal of dorsal iAChR clusters in *dve-1* mutants (**Figure S7.2D**). Likewise, a null mutation in *atfs-1* did not alter synapse elimination in otherwise wild-type animals and failed to restore synapse elimination when combined with mutation of *dve-1* in *atfs-1;dve-1* double mutants (**Figure 7B**). These results show that increased activation of the mtUPR in *dve-1* mutants is not sufficient to account for a failure in synapse removal. Consistent with this interpretation, we note that mutation of *ulp-4* suppresses mtUPR activation but disrupts synapse elimination (**Figure 6D-F; Figure S7.2B**). Constitutive mtUPR activation by mutation of the mitochondrial complex III subunit gene *isp-1* also did not alter synapse elimination (**Figure 7B; Figure S7.2C**) [60]. Additionally, mutation of *ubl-5*, a cofactor with DVE-1 in the initiation of the intestinal mtUPR [61], did not affect synapse elimination (**Figure 7B**). Our findings demonstrate that mtUPR activation or inhibition do not alter synapse removal. We conclude that DVE-1 coordinates synapse elimination through transcriptional regulation of alternate pathways, perhaps those identified from our enrichment analysis.

Given recent evidence for the regulation of synapse structure through ubiquitin-dependent degradation processes and links with neurological disease [62], we next asked whether DVE-1 control of synapse elimination may occur through transcriptional regulation of the ubiquitin-proteasome system. Using quantitative RT-PCR, we first investigated the expression of selected putative DVE-1 targets involved in UPS function. The expression of three of the four genes we tested (*cul-5*, *eel-1*, *spat-3*) was significantly altered in *dve-1* mutants (**Figure S7.2E**), suggesting DVE-1 regulation of their expression. We next investigated involvement of the UPS during synapse elimination using bortezomib, a small molecule inhibitor of the 26S proteasome. Treatment with high (≥10 μM) concentrations of bortezomib produced larval arrest. In contrast, treatment with 5 μM bortezomib disrupted UPS function, as assessed by induction of the *skn-1* dependent proteasome reporter *rpt-3pr::*GFP [63] (**Figure S7.2F**), but did not cause developmental arrest or appreciably reduce dendritic spines in mature DD neurons (**Figure S7.2G**). Notably, treatment with 5 μM bortezomib significantly delayed synapse elimination during remodeling. More than 50% of animals treated with bortezomib failed to remove juvenile dorsal postsynaptic sites in DD neurons by 24 hours after hatch (**Figure 7C,D**), suggesting a requirement for UPS function in synapse elimination. Given the potential for redundant functions amongst the putative UPS DVE-1 targets we identified, we asked if synapse elimination was affected in animals carrying a temperature-sensitive allele of the sole *C. elegans* E1 ubiquitin ligase, *uba-1* [64]. We found that synapse elimination was significantly delayed in *uba-1* mutants shifted to the restrictive temperature at 10 hours after hatch (**Figure 7E,F**), but was unaffected in animals raised continuously at the permissive temperature. While additional DVE-1 regulated pathways likely contribute, our identification and analysis of UPS pathway genes as potential targets for direct transcriptional regulation by DVE-1 lead us to propose that cell-autonomous DVE-1 transcriptional regulation of the ubiquitin proteasome system may be an important step for synapse elimination during remodeling (**Figure 7G**).

Discussion

Developmental remodeling of synaptic connectivity occurs throughout phylogeny, refining and reorganizing neuronal connections toward the establishment of the mature nervous system. While neuron-extrinsic events that shape remodeling, for example, microglial phagocytosis of synaptic material [5-8], have gained a lot of recent attention, neuron-intrinsic processes governing remodeling have remained less well-described. Likewise, the relationship between degenerative and growth processes during remodeling has not been clearly elucidated. The developmental remodeling of *C. elegans* GABAergic DD neurons presents a uniquely accessible system for addressing important questions about evolutionarily conserved neuron-intrinsic mechanisms of remodeling because the reorganization of their connectivity occurs without gross morphological changes or a requirement for synaptic removal by other cell types.

Here, we show that the homeodomain transcription factor DVE-1 is specifically required for the elimination of juvenile synaptic inputs to DD neurons during remodeling. In *dve-1* mutants, juvenile postsynaptic sites and apposing cholinergic presynaptic terminals are preserved into adulthood. The failure to eliminate these sites results in elevated activity at these synapses and impaired motor function. Interestingly, *dve-1* is not required for the growth of new DD neuron synaptic inputs that are characteristic of the mature motor circuit, indicating that the formation of new connections is not dependent upon elimination of pre-existing juvenile synapses. Likewise, mutation of *dve-1* does not alter developmental reorganization of synaptic outputs from DD neurons onto muscles. In *dve-1* mutants, newly relocated GABAergic synaptic terminals occupy similar territories in DD neurons as lingering juvenile synaptic inputs. Thus, the formation of new GABAergic presynaptic terminals during maturation of the circuit is not contingent on elimination of nearby juvenile postsynaptic sites in DD neurons.

Our findings lead us to propose that cell-autonomous transcriptional regulation of GABAergic

neurons by DVE-1 promotes the elimination of their juvenile synaptic inputs. We found that DVE-1 is expressed in a limited number of neurons, including GABAergic motor neurons, and DVE-1 localization to GABAergic nuclei is required for synapse elimination to proceed normally. DVE-1 regulation of synapse elimination shares interesting parallels with a previously described pathway for elimination of postsynaptic structures at mouse glutamatergic synapses through transcriptional regulation by Myocyte Enhancer Factor 2 (Mef2) [65, 66]. However, in contrast to MEF2-regulated synapse elimination, we found that DVE-1-dependent elimination is not strongly activity-dependent. Also, we did not observe strong temporal regulation of DVE-1 expression in GABAergic neurons prior to or during remodeling, raising important mechanistic questions about the timing of synapse elimination. One possible route for temporal regulation might be through control of DVE-1 nuclear localization. We show that DVE-1 localization to GABAergic nuclei can be regulated through SUMOylation. However, we observed nuclear localization of DVE-1 in GABAergic neurons prior to the onset of remodeling, suggesting the presence of additional mechanisms for temporal control. This is consistent with prior work indicating that temporally controlled expression of OIG-1 regulates the timing of remodeling [23, 24]. We found that precocious synapse elimination in *oig-1* mutants is reversed when *dve-1* function is also disrupted, further indicating that DVE-1 transcriptional regulation is required for synapse elimination to occur. In contrast, precocious growth of new synapses in *oig-1* mutants was not altered by mutation of *dve-1*, suggesting that DVE-1 regulated degenerative mechanisms act in parallel with growth processes that are regulated independently.

Our experiments show that mutation of *dve-1* affects the stability of both postsynaptic sites in DD GABAergic neurons and presynaptic terminals in cholinergic neurons. We show that the juvenile synaptic vesicle assemblies in axons of presynaptic cholinergic neurons are almost completely exchanged during the 10-hour period of wild type remodeling. This turnover of synaptic vesicles during wild-type remodeling contrasts with their relative stability over the 10 hours immediately

following remodeling. Notably, the turnover of juvenile cholinergic synaptic vesicle assemblies during remodeling is strikingly reduced in *dve-1* mutants, indicating that disruption of DVE-1 transcriptional activity is sufficient to stabilize presynaptic vesicle pools in cholinergic neurons. Since DVE-1 expression is limited to postsynaptic GABAergic neurons, our results suggest that DVE-1-regulated postsynaptic pathways promote exchange or elimination of juvenile presynaptic elements through destabilization of the postsynaptic apparatus and associated signaling components. Our photoconversion experiments also show that recruitment of new synaptic vesicles in cholinergic axons of *dve-1* mutants is not halted by the stabilization of juvenile synaptic vesicle assemblies. We noted an overall increase in dorsal synaptic vesicle material in *dve-1* mutants compared with either wild type or ventral synapses of *dve-1* mutants. We speculate that the retention of juvenile synaptic vesicle clusters in *dve-1* mutants occurs in parallel with the formation of new synaptic connections between cholinergic DA/B motor neurons and post-embryonic born VD GABAergic neurons. The increased synaptic vesicle material in dorsal cholinergic axons of *dve-1* mutants may therefore arise from the additive effects of these two processes. Our Ca^{2+} imaging and behavioral experiments provide evidence that the increase in cholinergic synaptic vesicles of dorsally projecting motor neurons alters circuit function such that cholinergic activation of dorsal musculature is enhanced in *dve-1* mutants, resulting in deeper dorsal bends and a dorsal turning bias during movement.

Our pathway analysis of DVE-1 ChIP-seq data showed enrichment of genes involved in the mtUPR. In the mtUPR, DVE-1/SATB is thought to organize loose chromatin to induce expression of chaperones and proteases [31, 58, 61]. However, manipulations that either activated or inhibited the mtUPR did not affect remodeling, providing support for a model where DVE-1 regulation of remodeling occurs independently of the mtUPR. Our analysis of potential DVE-1 targets revealed enrichment of genes in other pathways that may be important for the removal of synapses, in particular UPS pathway genes. Notably, pharmacological inhibition of proteasome

function or genetic disruption of *uba-1* caused a striking delay in synapse elimination, supporting involvement of this pathway and suggesting that DVE-1 transcriptional regulation of the proteasome may be important to promote synapse elimination. We note that potential synaptic targets for direct DVE-1 regulation were also present in the ChIP-seq dataset (**Supplemental file 5**), perhaps suggesting several modes of regulation. For example, UNC-40 has been shown to organize synapses through the MADD-4 ligand [67, 68] and is important for sexually dimorphic synapse pruning [69].

The closest homolog of DVE-1 is the *Drosophila* homeodomain transcription factor *defective proventriculus* (*Dve*). Interestingly, transcriptional profiling of *Drosophila* mushroom body gamma neurons during their remodeling showed Dve expression peaks at the onset of remodeling (https://www.weizmann.ac.il/mcb/Schuldiner/resources) [70]. DVE-1 also shares homology with the mammalian SATB proteins 1 and 2. SATB transcription factors have roles in many areas of mammalian brain development, such as the activation of immediate early genes important for maintaining dendritic spines in GABAergic interneurons [71] and cortex development and maturation [72], but roles in synapse elimination had been previously uncharacterized. Our findings offer a striking example of DVE-1/SATB transcriptional activation of pro-degenerative pathways acting in concert with temporally controlled expression of a maintenance factor to control a developmentally defined period of synapse elimination. Given the sequence similarities between DVE-1 and mammalian SATB proteins, our analysis may point toward new mechanisms by which SATB family transcription factors control brain development. Importantly, dysfunction of these transcription factors in humans, as in SATB2-associated syndrome, is characterized by significant neurodevelopmental delays, limitations in speech, and severe intellectual disability [25, 26]. More broadly, our findings highlight a cellular strategy for temporal control of circuit development through convergent regulation of antagonistic cellular processes. Interestingly, spatiotemporal regulation through competing parallel transcriptional programs is utilized in other

developmental contexts across different species [73-75], suggesting this represents a broadly utilized mechanism for temporal control of key developmental events.

Methods

Strains and Genetics

All strains are derivatives of the N2 Bristol strain (wild type) and maintained under standard conditions at 20-25°C on nematode growth media plates (NGM) seeded with *E. coli* strain OP50. Some strains were provided by the *Caenorhabditis* Genetics Center (CGC), which is funded by NIH Office of Research Infrastructure Programs (P40 OD010440), and by the National BioResource Project which is funded by the Japanese government. Transgenic strains were generated by microinjection of plasmids or PCR products into the gonad of young hermaphrodites. Integrated lines were produced by X-ray irradiation or UV-integration and outcrossed to wild type/N2 Bristol. A complete list of all strains used in this work is included in **supplemental file 1**.

Generation of Endogenously Tagged Strains

Strain PHX7515 ***dve-1(syb7515***) [DVE-1pr::AID::mScarlet] was generated in N2 animals by SunyBiotech. Linker, AID, and mScarlet sequences were inserted after exon 9 at the 3' end of ZK1193.5a.1/*dve-1.* Strain IZ4473 *dve-1(uf206)* was generated in *syb1984* (DVE-1 CRISPR-Cas9-mediated GFP knockin, gifted by the Tian lab) animals. A lysine to arginine (K-R) mutation was created by changing AAA to CGT in exon 6, 4783 bp downstream of start. The IDT CRISPR HDR design tool (https://www.idtdna.com/pages/tools/alt-r-crispr-hdr-design-tool) was used to generate repair templates and guide sequences. Animals were injected with CRISPR/Cas9 mix [crRNA (oligo 2 nmol, IDT), donor (oligo 4 nmol, IDT), purified Alt-R S.p. Cas9 nuclease V3 100µg (IDT CAT 1081058), Alt-R CRISPR/Cas9 tracrRNA (5 nmol, IDT CAT 1072532), and pRF-4 (*rol-6* plasmid)]. Rolling worms were singled and validated by PCR sequencing. CRISPR/Cas9 design is provided in **supplemental file 4**.

Molecular Biology

Plasmids were constructed using two-slot Gateway Cloning system (Invitrogen) and confirmed by restriction digest and/or sequencing as appropriate. All plasmids and primers used in this work are described in **supplemental files 2 and 3** respectively.

For *dve-1* genomic rescue, the *dve-1* promoter (5 kb upstream from translational start site), genomic fragment (from translational start to stop, 6107bp), and *dve-1* 3' UTR (626 bp downstream from translational stop) were amplified from genomic N2 DNA. For *dve-1* GABA-specific rescue, DVE-1 long (ZK1193.a) and short (ZK1193.c) isoform cDNA was amplified from RNA and ligated into SacII digested pCL86 and XbaI digested pCL101, respectfully to generate pDest-178 (*dve-1* cDNAa) and pDest-252 (*dve-1* cDNAc). pDest-178 and pDest-252 were recombined with pENTR-*unc-47* to generate pKA17 (*unc-47pr*:: *dve-1*a) and pJR21(*unc-47pr*:: *dve-1*c). pKA17 and pJR21 were injected simultaneously (30 ng/µl).

pKA110 (*unc-129pr*::Dendra2::RAB-3) was created by ligating a gBlock (IDT) containing the Dendra2 coding sequence into NheI-HF/PstI-HF digested pDest-114 to generate pDest-339 (Dendra2::RAB-3). pDest-339 was then recombined with pENTR-*unc-129* to generate pKA110 and injected at 50 ng/µl. To generate pKA35 (*unc-129pr*::Chrimson::SL2::BFP), Chrimson was amplified from pDest-104 and ligated into NheI-HF/BstBI digested pDest-239 to generate pDest-240 (Chrimson::SL2::BFP). pDest-240 was then recombined with pENTR-*unc-129* to generate pKA35 and injected at 50 ng/µl.

To generate *ulp-4* rescue constructs, *ulp-4* cDNA was amplified from RNA and ligated into NheI-HF/KpnI-HF digested pDest-139 to generate pDest-291. pDest-291 was recombined with pENTR-*unc-47* to generate pKA76 (*unc-47pr::ulp-4* cDNA), pENTR-F25B3.3 to generate pKA78 (*F25B3.3pr:: ulp-4* cDNA), and pENTR-*gly-19* to generate pKA80 (*gly-19pr:: ulp-4* cDNA). All *ulp-4* rescue constructs were injected at 30 ng/µl.

pKA74 (*unc-47pr*::NLS::mCherry) was created by amplifying an artificial intron and NLS from plasmid #68120 (Addgene) and was ligated into AgeI-HF/XbaI digested pDest-145 to generate pDest-205 (NLS::mCherry). pDest-205 was recombined with pENTR-*unc-47* to generate pKA74 and injected at 50 ng/µl.

pJR18 (Δ*dve-1pr*::DVE-1::GFP) was generated by ligating a gBlock (IDT) containing the *dve-1* promoter missing 6 putative UNC-30 binding sites (1214-1224, 1407-1417, 1456-1466, 1597-1607, 1634-1644, and 1782-1792 bp upstream of the *dve-1* start and ligated into into PsiI/SacI cut *dve-1pr*::DVE-1::GFP (plasmid gifted to us by Cole Haynes). pJR18 was injected at 5 ng/µl in N2 animals.

Staging time course for DD remodeling

Briefly, freshly hatched larvae were transferred to seeded OP50 plates and maintained at 25°C (timepoint 0). Imaging and analysis of iAChR or synaptic vesicle remodeling was assessed as previously described [23].

Confocal imaging and analysis

Unless noted otherwise, all strains were immobilized with sodium azide (0.3 M) on a 2% or 5% agarose pad. All confocal Images were obtained either using a Yokagawa CSU-10 spinning disk confocal equipped with a 63x objective or a Yokogawa CSU-X1-A1N spinning disk confocal (Perkin Elmer) equipped with EM-CCD camera (Hamamatsu, C9100-50) and 63x oil immersion objective. Analysis of synapse number and fluorescence intensity was performed using FIJI ImageJ software (open source) using defined threshold values acquired from control experiments for each fluorescent marker. Statistical analysis for all synaptic and spine analysis between two

groups utilized a student's t-test; for analysis where, multiple groups were compared either a one-way or two-way ANOVA was used with the appropriate *post hoc* test.

Synaptic analysis: Background fluorescence was subtracted by calculating the average intensity in a region outside the ROI. All ROIs were 25 µm or 30 µm in length. Quantification of the number of puncta within an ROI had a set threshold of 25-255 and the analyze particles function of ImageJ was used to quantify any particle greater than 4 pixels^2. Fluorescence intensity was quantified from the raw integrated fluorescence within the ROI. For quantification of DD neuron synapses, the ROI was defined as either the ventral region anterior to the DD1 soma or the opposing dorsal region. For quantification of the DA/DB neuron synapses the ROI was defined as either the ventral region between DB1 and DB3 or the opposing dorsal region between VB1 and VB3.

Spine/dendrite analysis: Spine number was quantified as described previously [27, 38]. Briefly, spines were counted within a 30 µm ROI anterior to the soma of DD1. Dendrite length was defined as the anterior extension from DD1 soma to the end of the ventral process.

EMS screen

The EMS mutagenesis protocol was adapted from [76]. Strain IZ1905 (*flp-13pr::*ACR-12::GFP) was treated with 25 µM ethyl methanesulfonate (EMS, Sigma). After washing, P0 mutagenized animals were recovered. F1 animals were transferred to fresh plates and 8 F2s were isolated per F1 (F2 clonal screen). The F3 progeny of ~400 F2s per round were screened. After 27 rounds of EMS, a total of 3261 haploid genomes were screened. Each isolated candidate mutant was rescreened three times to confirm the phenotype.

Variant discovery mapping and whole genome sequencing

Mutant strains were backcrossed a single time into the starting strain injected with *unc-122pr::*GFP co-injection marker (IZ2302, enabling the distinction of cross- from self-progeny). F2 animals were isolated onto separate plates and their F3 brood were screened by confocal microscope for synapse elimination. 21 independent homozygous recombinant F2 lines were isolated and pooled together. Worm genomic DNA was prepared for sequencing using Gentra Puregene Tissue Kit DNA purification (Qiagen). Library construction and whole genome sequencing were performed by Novogene. Briefly, NEBNext DNA Library Prep Kit was used for library construction. Pair-end sequencing was performed on Illumina sequencing platform with a read length of 150 bp at each end. Reads were mapped to *C. elegans* reference genome version WS220 and analyzed using the CloudMap pipeline [77] where mismatches were compared to the parental strain as well as to other mutants isolated from the screen [77, 78].

Auxin treatment

NGM control (ethanol) or 4 mM synthetic auxin analog 1 (NAA) (Sigma-Aldrich CAS:317918) plates were made as described [32, 33, 79]. Plates were seeded with concentrated OP50 and stored at room temperature and kept out of light. Animals were synchronized at hatch and staged onto either control or NAA plates.

Injection of fluorescent antibodies for *in vivo* labeling of iAChRs

Mouse monoclonal α-HA antibodies (16B12 Biolegend) coupled to Alexa594 were diluted in injection buffer (20 mM K_3PO_4, 3 mM K citrate, 2% PEG 6000, pH 7.5). Antibody was injected into the pseudocoelom of L2/L3 stage wild type or *dve-1(uf171)* animals as described previously [23, 39]. Animals were allowed to recover for six hours on seeded NGM plates. Only animals in which

fluorescence was observed in coelomocytes were included in the analysis. A student's t-test was used for statistical analysis.

Photoconversion of Dendra2::RAB-3

Wild-type and *dve-1(uf171)* mutant L1 animals (12-14 hours post-hatch) expressing Dendra2::RAB3 were paralyzed for imaging using 1 mM levamisole. Dendra2::RAB-3 puncta in the DA/DB dorsal axonal process were photoconverted using a 405 nm laser at 800 ms for 30 s. Images were acquired immediately following photoconversion and again 10 hours later. Animals were rescued following photoconversion and imaging, and allowed to recover until the subsequent timepoint. Both red and green fluorescent signals were quantified. A student's t-test was used for statistical analysis.

Aldicarb paralysis assays

Aldicarb assays were performed as previously [44]. Strains were scored in parallel, with the researcher blinded to the genotype. Young adult animals (24 hours after L4) at room temperature (22–24°C) were selected (>10 per trial for at least 3 trials) and transferred to a nematode growth medium plate containing 1 mM aldicarb (Sigma-Aldrich CAS:116-06-3). Movement was assessed every 15 minutes for 2 hours. Animals that displayed no movement when prodded (paralyzed) were noted. The percentage of paralyzed animals was calculated at each timepoint.

Calcium imaging

Transgenic animals expressing *ttr-39pr*::GCaMP6s::SL2::mCherry (GABA neurons) along with

676 *unc-129pr*::Chrimson::SL2::BFP (DA and DB cholinergic neurons) were grown on NGM plates
677 with OP50 containing 2.75 mM All-Trans Retinal (ATR). L4 animals (40 hours post-hatch) were
678 staged 24 hours prior to experiments on fresh ATR OP50 NGM plates. Imaging was performed
679 using 1-day adults immobilized in hydrogel [27, 80]. Animals were transferred to 7.5 µL of hydrogel
680 mix placed on a silanized glass slide and covered with a cover slip. Hydrogel was cured using a
681 handheld UV Transilluminator (312 nm, 3 minutes). A TTL-controlled 625 nm light guide coupled
682 LED (Mightex Systems) was used for Chrimson photoactivation (~14 mW/cm^2). A 556 nm
683 BrightLine single-edge short-pass dichroic beam splitter was positioned in the light path
684 (Semrock) [38]. Data were acquired at 10 Hz for 15 s using Volocity software with 4x4 binning.
685 Analysis was performed using ImageJ. DD and VD GABA motor neuron cell bodies were identified
686 by mCherry fluorescence and anatomically identified by position along the ventral nerve cord.
687 Each field typically contained 1–5 GABA motor neurons. Only neurons located anterior to the
688 vulva were included in the analysis. Photobleaching correction was performed on background
689 subtracted images by fitting an exponential function to the data (CorrectBleach plugin, ImageJ).
690 Pre-stimulus baseline fluorescence (F_0) was calculated as the average of the corrected
691 background-subtracted data points in the first 4 s of the recording and the corrected fluorescence
692 data were normalized to prestimulus baseline as $\Delta F/F_0$, where $\Delta F=F–F_0$. Peak $\Delta F/F_0$ was
693 determined by fitting a Gaussian function to the $\Delta F/F_0$ time sequence using Multi peak 2.0 (Igor
694 Pro, WaveMetrics). All data collected were analyzed, including failures (no response to
695 stimulation). Peak $\Delta F/F_0$ values were calculated from recordings of >10 animals per genotype.
696 Mean peaks ± SEM were calculated from all peak $\Delta F/F_0$ data values. For all genotypes, control
697 animals grown in the absence of ATR were imaged.

698

699 Single worm tracking

Single worm tracking was carried out on NGM plates seeded with 50 µL of OP50 bacteria, using Worm Tracker 2 [81]. Animals were acclimated for 30 s prior to tracking. Worm tracker software version 2.0.3.1, created by Eviatar Yemini and Tadas Jucikas (Schafer lab, MRC, Cambridge, UK), was used to analyze movement [82]. Locomotion paths and movement features were extracted from 5 minutes of continuous locomotion tracking. Scoring of path trajectories was performed blinded to genotype.

Optogenetic analysis

Behavioral assays were performed with young adults at room temperature (22°C–24°C). Animals were grown on plates seeded with OP50 containing 2.7 mM All-Trans Retinal (ATR). Animals were placed on fresh plates seeded with a thin lawn of OP50 containing ATR and allowed to acclimate for 1 minute. Dorsal-ventral position was noted prior to recording. Animals were allowed to move freely on plates and recorded with a Mightex X camera for 1 minute before stimulus, following this a Mightex LED module was used to stimulate Chrimson (625nm 14mW/cm^2) continuously for 2 minutes. Locomotion (trajectory and body bending) was analyzed with WormLab (MBF Bioscience) software. A mid-point bending angle histogram was generated for each animal such that over the span of 2 minutes body angles were measured and binned by the degree of angle. Depending on starting position, negative and positive degree angles were assigned dorsal or ventral. Any bending angle greater than 0 but less than 50˚ was determined a regular bend. We noted wild type animals without stimulus rarely make angles greater than 50˚ and qualified any bending angle over 50˚ as a deep bend. An ANOVA with Dunnett's multiple comparisons test was used for comparisons between pre-stimulus and stimulus in wild type and *dve-1(uf171)*. Student's t-test was used when comparing the number of dorsal bends greater than 50° in wildtype vs *dve-1* mutant animals.

RNAi by feeding

L4 larvae expressing *hsp-6pr::*GFP were cultured with *E. coli* expressing either control double-stranded RNA (empty vector) or targeting *atfs-1* and progeny were allowed to develop to L4 stage at 20°C. Intestinal GFP fluorescence of L4 stage progeny was measured using the Zeiss Imager M1, 10x objective.

DVE-1 nuclear localization

DVE-1::GFP was measured in L1 stage DD nuclei of *dve-1(syb1984)*; *ufEx1814*(*unc-47pr::NLS::mCherry*) animals. ROIs were determined by expression of the nuclear localized mCherry signal. Within the ROI a segmented line was drawn through the nucleus and an intensity profile was created for each nucleus. Fluorescence intensity values for DVE-1::GFP were quantified by averaging the largest 5 intensity values at the peak (roughly 0.5 µm). At least 2 DD nuclei per animal were analyzed. ANOVA with Dunnett's multiple comparison test was used for statistical analysis. For measurements in *unc-30* mutants, an ROI extending posteriorly 30 µm from the base of the pharynx was selected. Red GABA neurons in the head, unaffected by *unc-30* mutation, and the pharynx were used as landmarks. Students t-test was used for statistical analysis.

ChIP-seq data acquisition from ModEncode and de novo motif discovery

modENCODE (www.modencode.org) ChIP-seq data were generated by anti-GFP immunoprecipitation from animals stably expressing DVE-1::GFP (strain OP398). The DVE-1

ChIP-seq dataset included two biological replicates at the late embryo stage as well as control animals. Significant peaks were called using PeakSeq and only peaks that were identified in both biological replicates were considered for analysis. DVE-1::GFP ChIP-seq data and experimental details can be found at http://intermine.modencode.org/release-33/report.do?id=77000654 (DCCid: **modENCODE_4804)** [83, 84]. Peaks were considered mapped to genes if there was at least 80% overlap between the peak maximum read density and a 1 kb region upstream of transcriptional start site using the UCSC table browser intersect function [85]. DVE-1 peaks assigned to promoters were used for *de novo* motif discovery. The sequences of the complete peak region were retrieved from modENCODE. *De novo* motifs were identified using the peak-motifs module of RSAT (Regulatory Sequence Analysis Tools) [86, 87]

Pathway analysis

Pathway analysis was performed using both WormCat [56] (http://www.wormcat.com) and WormenrichR [57, 88] (https://amp.pharm.mssm.edu/WormEnrichr/). For WormCat analysis, pathways with p<0.01 and Bonferroni FDR<0.01 were considered enriched. The WormEnrichR pathway enrichment analysis utilized the WikiPathway database [89]. WormEnrichR uses the logarithm of the p-value from a Fischer exact test and multiplying that by the z-score of the expected rank to create a combined score. Pathways with adjusted p<0.05 and combined score >5 were considered enriched (Figure 7A).

RNA isolation and RT-qPCR

L1 N2 and *dve-1*(uf171) mutant animals were lysed in 2% SDS, 20% b-ME, 40 mM EDTA, 40 mM Tris-HCl pH 7.5, 2 mg/ml Proteinase K. RNA was isolated (Zymo CAS:R1013) and treated with DNAse (Roche CAS:4716728001). cDNA was prepared using reverse transcriptase (RT) synthesis (Roche CAS:5081955001 and Thermo CAS:SO142). RT-qPCR procedures were followed according to the KAPA SYBR FAST qPCR Kit protocol (CAS:7959397001) and

performed with a Bio-Rad CFX96 Real-Time System with a C1000 Touch Thermal Cycler. cDNA was standardized to *act-1*. Primers used are listed in supplemental file 3. Representative experiments from at least three repetitions are shown.

Proteasome and *uba-1* time course and experiments

Worms were hatched synchronously on NGM plates. Wild type animals were transferred to either 5 µM Bortezomib (MilliporeSignma CAS:179324-69-7) or control (DMSO) plates 10 hours after hatch and allowed to develop until imaging at 24 hours after hatch. Wildtype and *uba-1(it129)* mutants were either maintained continuously at 15°C or transferred from 15°C to 25°C at 10 hours after hatch and until imaging at 24 hours after hatch.

Statistics and Reproducibility

Summary statistics are included in supplementary file 6.

Data Availability

All raw data represented in this manuscript is provided in the Supplementary Information/Source Data file. DVE-1::GFP ChIP-seq data and experimental details can be found in the modENCODE project database at http://intermine.modencode.org/release-33/report.do?id=77000654 (DCCid: **modENCODE_4804)**

References

1. Crepel, F., J. Mariani, and N. Delhaye-Bouchaud, *Evidence for a multiple innervation of Purkinje cells by climbing fibers in the immature rat cerebellum.* Journal of neurobiology, 1976. **7**(6): p. 567-578.
2. Hong, Y.K., et al., *Refinement of the retinogeniculate synapse by bouton clustering.* Neuron, 2014. **84**(2): p. 332-339.
3. Hubel, D.H., et al., *Plasticity of ocular dominance columns in monkey striate cortex.* Philosophical Transactions of the Royal Society of London. B, Biological Sciences, 1977. **278**(961): p. 377-409.
4. Technau, G. and M. Heisenberg, *Neural reorganization during metamorphosis of the corpora pedunculata in Drosophila melanogaster.* Nature, 1982. **295**(5848): p. 405-407.
5. Paolicelli, R.C., et al., *Synaptic pruning by microglia is necessary for normal brain development.* science, 2011. **333**(6048): p. 1456-1458.
6. Schafer, D., et al., *Microglia sculpt postnatal neural circuits in an activity and complement-dependent manner.* Neuron, 2012. **74**(4): p. 691-705.
7. Tremblay, M.-È., R.L. Lowery, and A.K. Majewska, *Microglial interactions with synapses are modulated by visual experience.* PLoS biology, 2010. **8**(11): p. e1000527.
8. Wake, H., et al., *Resting microglia directly monitor the functional state of synapses in vivo and determine the fate of ischemic terminals.* Journal of Neuroscience, 2009. **29**(13): p. 3974-3980.
9. Kobayashi, Y., Z. Ye, and T.K. Hensch, *Clock genes control cortical critical period timing.* Neuron, 2015. **86**(1): p. 264-275.
10. Hong, S., et al., *Complement and microglia mediate early synapse loss in Alzheimer mouse models.* Science, 2016. **352**(6286): p. 712-716.
11. Knobloch, M. and I.M. Mansuy, *Dendritic spine loss and synaptic alterations in Alzheimer's disease.* Molecular neurobiology, 2008. **37**(1): p. 73-82.
12. Sekar, A., et al., *Schizophrenia risk from complex variation of complement component 4.* Nature, 2016. **530**(7589): p. 177-183.
13. Yaron, A. and O. Schuldiner, *Common and divergent mechanisms in developmental neuronal remodeling and dying back neurodegeneration.* Current Biology, 2016. **26**(13): p. R628-R639.
14. Sulston, J.E., *Post-embryonic development in the ventral cord of Caenorhabditis elegans.* Philosophical Transactions of the Royal Society of London. B, Biological Sciences, 1976. **275**(938): p. 287-297.
15. White, J.G., et al., *The structure of the nervous system of the nematode Caenorhabditis elegans.* Philos Trans R Soc Lond B Biol Sci, 1986. **314**(1165): p. 1-340.
16. Cuentas-Condori, A. and r. Miller, David M, *Synaptic remodeling, lessons from C. elegans.* Journal of neurogenetics, 2020. **34**(3-4): p. 307-322.
17. White, J.G., D. Albertson, and M. Anness, *Connectivity changes in a class of motoneurone during the development of a nematode.* Nature, 1978. **271**(5647): p. 764-766.

18. Hallam, S.J. and Y. Jin, *lin-14 regulates the timing of synaptic remodelling in Caenorhabditis elegans.* Nature, 1998. **395**(6697): p. 78-82.
19. Miller-Fleming, T.W., et al., *The DEG/ENaC cation channel protein UNC-8 drives activity-dependent synapse removal in remodeling GABAergic neurons.* Elife, 2016. **5**: p. e14599.
20. Park, M., et al., *CYY-1/cyclin Y and CDK-5 differentially regulate synapse elimination and formation for rewiring neural circuits.* Neuron, 2011. **70**(4): p. 742-757.
21. Thompson-Peer, K.L., et al., *HBL-1 patterns synaptic remodeling in C. elegans.* Neuron, 2012. **73**(3): p. 453-465.
22. Mulcahy, B., et al., *Post-embryonic remodeling of the C. elegans motor circuit.* Current Biology, 2022.
23. He, S., et al., *Transcriptional control of synaptic remodeling through regulated expression of an immunoglobulin superfamily protein.* Current Biology, 2015. **25**(19): p. 2541-2548.
24. Howell, K., J.G. White, and O. Hobert, *Spatiotemporal control of a novel synaptic organizer molecule.* Nature, 2015. **523**(7558): p. 83-87.
25. Den Hoed, J., et al., *Mutation-specific pathophysiological mechanisms define different neurodevelopmental disorders associated with SATB1 dysfunction.* The American Journal of Human Genetics, 2021. **108**(2): p. 346-356.
26. Zarate, Y.A., et al., *Natural history and genotype‐phenotype correlations in 72 individuals with SATB2‐associated syndrome.* American Journal of Medical Genetics Part A, 2018. **176**(4): p. 925-935.
27. Oliver, D., et al., *Kinesin-3 mediated axonal delivery of presynaptic neurexin stabilizes dendritic spines and postsynaptic components.* PLoS genetics, 2022. **18**(1): p. e1010016.
28. Petrash, H.A., et al., *ACR-12 ionotropic acetylcholine receptor complexes regulate inhibitory motor neuron activity in Caenorhabditis elegans.* Journal of Neuroscience, 2013. **33**(13): p. 5524-5532.
29. Meng, L., et al., *The cell death pathway regulates synapse elimination through cleavage of gelsolin in Caenorhabditis elegans neurons.* Cell reports, 2015. **11**(11): p. 1737-1748.
30. Jumper, J., et al., *Highly accurate protein structure prediction with AlphaFold.* Nature, 2021. **596**(7873): p. 583-589.
31. Haynes, C.M., et al., *ClpP mediates activation of a mitochondrial unfolded protein response in C. elegans.* Developmental cell, 2007. **13**(4): p. 467-480.
32. Nishimura, K., et al., *An auxin-based degron system for the rapid depletion of proteins in nonplant cells.* Nature methods, 2009. **6**(12): p. 917-922.
33. Zhang, L., et al., *The auxin-inducible degradation (AID) system enables versatile conditional protein depletion in C. elegans.* Development, 2015. **142**(24): p. 4374-4384.
34. Reilly, M.B., et al., *Unique homeobox codes delineate all the neuron classes of C. elegans.* Nature, 2020. **584**(7822): p. 595-601.
35. Gally, C., et al., *A transmembrane protein required for acetylcholine receptor clustering in Caenorhabditis elegans.* Nature, 2004. **431**(7008): p. 578-582.

36. He, S., A. Cuentas-Condori, and D.M. Miller III, *NATF (Native and Tissue-Specific Fluorescence): a strategy for bright, tissue-specific GFP labeling of native proteins in Caenorhabditis elegans.* Genetics, 2019. **212**(2): p. 387-395.
37. Cuentas-Condori, A., et al., *C. elegans neurons have functional dendritic spines.* Elife, 2019. **8**: p. e47918.
38. Philbrook, A., et al., *Neurexin directs partner-specific synaptic connectivity in C. elegans.* elife, 2018. **7**: p. e35692.
39. Gottschalk, A. and W.R. Schafer, *Visualization of integral and peripheral cell surface proteins in live Caenorhabditis elegans.* Journal of neuroscience methods, 2006. **154**(1-2): p. 68-79.
40. Klapoetke, N.C., et al., *Independent optical excitation of distinct neural populations.* Nature methods, 2014. **11**(3): p. 338-346.
41. Larsch, J., et al., *A circuit for gradient climbing in C. elegans chemotaxis.* Cell reports, 2015. **12**(11): p. 1748-1760.
42. Chen, T.-W., et al., *Ultrasensitive fluorescent proteins for imaging neuronal activity.* Nature, 2013. **499**(7458): p. 295-300.
43. Varshney, L.R., et al., *Structural properties of the Caenorhabditis elegans neuronal network.* PLoS computational biology, 2011. **7**(2): p. e1001066.
44. Nguyen, M., et al., *Caenorhabditis elegans mutants resistant to inhibitors of acetylcholinesterase.* Genetics, 1995. **140**(2): p. 527-535.
45. Zhu, D., et al., *NuRD mediates mitochondrial stress–induced longevity via chromatin remodeling in response to acetyl-CoA level.* Science advances, 2020. **6**(31): p. eabb2529.
46. Cinar, H., S. Keles, and Y. Jin, *Expression profiling of GABAergic motor neurons in Caenorhabditis elegans.* Current Biology, 2005. **15**(4): p. 340-346.
47. Shan, G., et al., *Convergent genetic programs regulate similarities and differences between related motor neuron classes in Caenorhabditis elegans.* Developmental biology, 2005. **280**(2): p. 494-503.
48. Yu, B., et al., *Convergent transcriptional programs regulate cAMP levels in C. elegans GABAergic motor neurons.* Developmental Cell, 2017. **43**(2): p. 212-226. e7.
49. Gao, K., et al., *SUMO peptidase ULP-4 regulates mitochondrial UPR-mediated innate immunity and lifespan extension.* Elife, 2019. **8**: p. e41792.
50. Dobreva, G., J. Dambacher, and R. Grosschedl, *SUMO modification of a novel MAR-binding protein, SATB2, modulates immunoglobulin μ gene expression.* Genes & development, 2003. **17**(24): p. 3048-3061.
51. Tan, J.-A.T., et al., *Phosphorylation-dependent interaction of SATB1 and PIAS1 directs SUMO-regulated caspase cleavage of SATB1.* Molecular and cellular biology, 2010. **30**(11): p. 2823-2836.
52. Boyle, A.P., et al., *Comparative analysis of regulatory information and circuits across distant species.* Nature, 2014. **512**(7515): p. 453-456.
53. Shao, L.-W., et al., *Histone deacetylase HDA-1 modulates mitochondrial stress response and longevity.* Nature communications, 2020. **11**(1): p. 1-12.
54. Hammarlund, M., et al., *The CeNGEN project: the complete gene expression map of an entire nervous system.* Neuron, 2018. **99**(3): p. 430-433.

55. Taylor, S.R., et al., *Molecular topography of an entire nervous system.* Cell, 2021. **184**(16): p. 4329-4347. e23.
56. Holdorf, A.D., et al., *WormCat: an online tool for annotation and visualization of Caenorhabditis elegans genome-scale data.* Genetics, 2020. **214**(2): p. 279-294.
57. Kuleshov, M.V., et al., *Enrichr: a comprehensive gene set enrichment analysis web server 2016 update.* Nucleic acids research, 2016. **44**(W1): p. W90-W97.
58. Tian, Y., et al., *Mitochondrial stress induces chromatin reorganization to promote longevity and UPRmt.* Cell, 2016. **165**(5): p. 1197-1208.
59. Wu, Z., et al., *Mitochondrial unfolded protein response transcription factor ATFS-1 promotes longevity in a long-lived mitochondrial mutant through activation of stress response pathways.* BMC biology, 2018. **16**(1): p. 1-19.
60. Yang, W. and S. Hekimi, *A mitochondrial superoxide signal triggers increased longevity in Caenorhabditis elegans.* PLoS biology, 2010. **8**(12): p. e1000556.
61. Benedetti, C., et al., *Ubiquitin-like protein 5 positively regulates chaperone gene expression in the mitochondrial unfolded protein response.* Genetics, 2006. **174**(1): p. 229-239.
62. Cheon, S., M. Dean, and M. Chahrour, *The ubiquitin proteasome pathway in neuropsychiatric disorders.* Neurobiology of learning and memory, 2019. **165**: p. 106791.
63. Lehrbach, N.J. and G. Ruvkun, *Proteasome dysfunction triggers activation of SKN-1A/Nrf1 by the aspartic protease DDI-1.* elife, 2016. **5**: p. e17721.
64. Kulkarni, M. and H.E. Smith, *E1 ubiquitin-activating enzyme UBA-1 plays multiple roles throughout C. elegans development.* PLoS genetics, 2008. **4**(7): p. e1000131.
65. Chang, C.-W., et al., *Distinct stages of synapse elimination are induced by burst firing of CA1 neurons and differentially require MEF2A/D.* Elife, 2017. **6**: p. e26278.
66. Flavell, S.W., et al., *Activity-dependent regulation of MEF2 transcription factors suppresses excitatory synapse number.* Science, 2006. **311**(5763): p. 1008-1012.
67. Tu, H., et al., *C. elegans punctin clusters GABAA receptors via neuroligin binding and UNC-40/DCC recruitment.* Neuron, 2015. **86**(6): p. 1407-1419.
68. Platsaki, S., et al., *The Ig-like domain of Punctin/MADD-4 is the primary determinant for interaction with the ectodomain of neuroligin NLG-1.* Journal of Biological Chemistry, 2020. **295**(48): p. 16267-16279.
69. Salzberg, Y., et al., *Synaptic protein degradation controls sexually dimorphic circuits through regulation of DCC/UNC-40.* Current biology, 2020. **30**(21): p. 4128-4141. e5.
70. Alyagor, I., et al., *Combining developmental and perturbation-seq uncovers transcriptional modules orchestrating neuronal remodeling.* Developmental cell, 2018. **47**(1): p. 38-52. e6.
71. Balamotis, M.A., et al., *Satb1 ablation alters temporal expression of immediate early genes and reduces dendritic spine density during postnatal brain development.* Molecular and cellular biology, 2012. **32**(2): p. 333-347.
72. Turovsky, E.A., et al., *Role of Satb1 and Satb2 transcription factors in the glutamate receptors expression and Ca2+ signaling in the cortical neurons in vitro.* International journal of molecular sciences, 2021. **22**(11): p. 5968.

73. di Sanguinetto, S.A.D.T., J.S. Dasen, and S. Arber, *Transcriptional mechanisms controlling motor neuron diversity and connectivity.* Current opinion in neurobiology, 2008. **18**(1): p. 36-43.
74. Srinivasan, K., et al., *A network of genetic repression and derepression specifies projection fates in the developing neocortex.* Proceedings of the National Academy of Sciences, 2012. **109**(47): p. 19071-19078.
75. Viets, K., K.C. Eldred, and R.J. Johnston Jr, *Mechanisms of photoreceptor patterning in vertebrates and invertebrates.* Trends in Genetics, 2016. **32**(10): p. 638-659.
76. Jorgensen, E.M. and S.E. Mango, *The art and design of genetic screens: Caenorhabditis elegans.* Nature Reviews Genetics, 2002. **3**(5): p. 356-369.
77. Minevich, G., et al., *CloudMap: a cloud-based pipeline for analysis of mutant genome sequences.* Genetics, 2012. **192**(4): p. 1249-1269.
78. Doitsidou, M., S. Jarriault, and R.J. Poole, *Next-generation sequencing-based approaches for mutation mapping and identification in Caenorhabditis elegans.* Genetics, 2016. **204**(2): p. 451-474.
79. Kurashina, M. and K. Mizumoto, *Targeting endogenous proteins for spatial and temporal knockdown using auxin-inducible degron in Caenorhabditis elegans.* STAR protocols, 2023. **4**(1): p. 102028.
80. Burnett, K., E. Edsinger, and D.R. Albrecht, *Rapid and gentle hydrogel encapsulation of living organisms enables long-term microscopy over multiple hours.* Communications biology, 2018. **1**(1): p. 1-10.
81. Yemini, E., R.A. Kerr, and W.R. Schafer, *Preparation of samples for single-worm tracking.* Cold Spring Harbor Protocols, 2011. **2011**(12): p. pdb. prot066993.
82. Yemini, E., et al., *A database of Caenorhabditis elegans behavioral phenotypes.* Nature methods, 2013. **10**(9): p. 877-879.
83. Gerstein, M.B., et al., *Integrative analysis of the Caenorhabditis elegans genome by the modENCODE project.* Science, 2010. **330**(6012): p. 1775-1787.
84. Sarov, M., et al., *A genome-scale resource for in vivo tag-based protein function exploration in C. elegans.* Cell, 2012. **150**(4): p. 855-866.
85. Karolchik, D., et al., *The UCSC Table Browser data retrieval tool.* Nucleic acids research, 2004. **32**(suppl_1): p. D493-D496.
86. Thomas-Chollier, M., et al., *RSAT 2011: regulatory sequence analysis tools.* Nucleic acids research, 2011. **39**(suppl_2): p. W86-W91.
87. Thomas-Chollier, M., et al., *RSAT peak-motifs: motif analysis in full-size ChIP-seq datasets.* Nucleic acids research, 2012. **40**(4): p. e31-e31.
88. Chen, E.Y., et al., *Enrichr: interactive and collaborative HTML5 gene list enrichment analysis tool.* BMC bioinformatics, 2013. **14**(1): p. 1-14.
89. Martens, M., et al., *WikiPathways: connecting communities.* Nucleic acids research, 2021. **49**(D1): p. D613-D621.

Acknowledgements

We thank Alexandra Byrne, Dori Schafer and the members of the Francis lab for critical reading of the manuscript. We also thank Ye Tian and Cole Haynes for generously sharing reagents and Michael Gorczyca and Will Joyce for technical assistance. We would like to thank Mark Alkema and Jeremy Florman for assistance with single worm tracking and analysis scripts. Some nematode strains were provided by the *Caenorhabditis* Genetics Center which is funded by the NIH National Center for Research Resources, and by the National Bioresource Project Nematode of Japan. This research was supported by NIH RO1NS064263 (MMF), HHMI Gilliam GT11432 (KA), and IMSD T32GM135701 (KA).

Author Contributions

KDA generated strains, transgenic lines, molecular constructs, confocal microscopy images and analysis, performed optogenetic behavioral experiments, photoconversion experiments, modencode ChIP-seq analysis and pathway analysis. SR performed all calcium imaging experiments/analysis and conducted single worm tracking. KB performed all Bortezomib inhibitor experiments and analysis. CL generated most vectors and constructs. JR assisted with generation of CRISPR/Cas9 generated strains. WA and MR assisted with aldicarb behavioral assay. CB and DO assisted with EMS screen and isolation of *dve-1* mutant. CB and MD aided in CloudMap bioinformatic analysis of the *uf171* mutant. SL and AKW performed and analyzed all qPCR experiments. MMF and KDA designed and interpreted results of all experiments and wrote the manuscript.

Competing Interests Declared: No competing interests declared

Table 1. Mutations that delay GABAergic presynaptic remodeling do not affect cholinergic postsynaptic remodeling in DD motor neurons

AChR (*flp-13pr*::ACR-12::GFP)					
genotype (L4 stage)	**percent remodeled (ventral only) (n)**	**percent not remodeled (dorsal only and both sides) (n)**	**total (n)**	**Fischer's Exact P-value (two-tailed)**	**Bonferroni Correction (significant?) α < 0.003**
wild type	100 (100)	0 (3)	103		
ced-3(ok2734)	100 (21)	0 (0)	21	1	no
ced-3(n717)	100 (23)	0 (0)	23	1	no
cdk-5(ok626)	100 (20)	0 (0)	20	1	no
unc-8(e49)	100 (20)	0 (0)	20	1	no
unc-8(e15)	100 (20)	0 (0)	20	1	no
SV (*flp-13pr*::mCherry::RAB-3)					
genotype (L4 stage)	**percent remodeled (ventral only) (n)**	**percent not remodeled (dorsal only and both sides) (n)**	**total (n)**	**Fischer's Exact P-value**	**Bonferroni Correction (significant?) α < 0.01**
wild type	100 (40)	0 (0)	40		
ced-3(ok2734)	56 (6)	44 (5)	11	0.0003	yes
ced-3(n717)	57 (13)	43 (10)	23	8.95E-06	yes
cdk-5(ok626)	24 (5)	76 (16)	21	1E-10	yes
unc-8(e49)	56 (9)	44 (7)	16	5E-05	yes
unc-8(e15)	62 (13)	38 (8)	21	0.0001	yes

1037 **Table 2. Effects of synaptic activity and calcium signaling on synaptic remodeling**

AChR (*flp-13pr*::ACR-12::GFP)					
genotype (24 hours post-hatch)	**percent remodeled (ventral only) (n)**	**percent not remodeled (dorsal only and both sides) (n)**	**total (n)**	**Fischer's Exact P-value (two-tailed)**	**Bonferroni Correction (significant?) α < 0.0055**
wild type	96 (64)	4 (3)	67		
unc-2(e55)	89 (16)	11 (2)	18	0.29	no
cca-1(ad1650)	100 (17)	0 (0)	17	1	no
itr-1(sa73)	100 (18)	0 (0)	18	1	no
unc-68(e540)	50 (10)	50 (10)	20	9.02E-06	yes
unc-13(e51)	100 (15)	0 (0)	15	1	no
unc-43(e408)	95 (19)	5 (1)	20	1	no
unc-18(e234)	100 (16)	0 (0)	16	1	no
unc-17(e113)	76 (13)	24 (4)	17	0.03	no
genotype (L4 stage)	**percent remodeled (ventral only) (n)**	**percent not remodeled (dorsal only and both sides) (n)**	**total (n)**	**Fischer's Exact P-value (two-tailed)**	**Bonferroni Correction (significant?) α < 0.003**
wild type	100 (93)	0 (0)	93		
unc-2(e55)	100 (20)	0 (0)	20	1	no
unc-2(zf35)	88 (15)	12 (2)	17	0.15	no
cca-1(ad1650)	100 (17)	0 (0)	17	1	no
itr-1(sa73)	90 (18)	10 (2)	20	0.18	no
unc-68(e540)	90 (19)	10 (2)	21	0.2	no
unc-43(e408)	95 (18)	5 (1)	19	0.17	no
unc-43(e498)	100 (15)	0 (0)	15	1	no
unc-18(e234)	100 (16)	0 (0)	16	1	no
unc-31(e928)	100 (20)	0 (0)	20	1	no
unc-17(e113)	100 (15)	0 (0)	15	1	no
AChR (*flp-13pr*::ACR-12::GFP)					
genotype (24 hours post-hatch)	**percent remodeled (ventral only) (n)**	**percent not remodeled (dorsal only and both sides) (n)**	**total (n)**	**Fischer's Exact P-value (two-tailed)**	**Bonferroni Correction (significant?) α < 0.025**
wild type	97 (28)	3 (1)	29		
unc-18(e234)	44 (7)	56 (9)	16	0.0001	yes
unc-17(e113)	33 (2)	67 (4)	6	0.0014	Yes

Figure legends

Figure 1. Mutation of the homeodomain transcription factor *dve-1* disrupts the removal of postsynaptic sites in GABAergic motor neurons

(A) Top, schematic of *C. elegans* indicating DD GABAergic motor neurons (purple). Bottom, schematic depicting motor circuit before (left) and after (right) remodeling. DD motor neurons (purple), cholinergic motor neurons (blue).

(B) Top, timeline of remodeling, approximate timing of transitions between larval stages and adulthood are indicated. Bars indicate the duration of DD synaptic remodeling for wild type (grey) and *dve-1* mutants (purple). Elimination of dorsal cord iAChR clusters is completed by 22 hours after hatch for wild type whereas dorsal iAChR clusters persist through adulthood in *dve-1* mutants. Middle, quantification of iAChR remodeling in DD neurons of wild type (left) and *dve-1* mutants (right). X-axis time from hatch in hours. Animals are binned according to the distribution of iAChR puncta as dorsal only (white), ventral only (black), or dorsal and ventral (grey). Bottom, representative images of dorsal and ventral ACR-12::GFP (iAChRs, green) clusters for wild type (left) and *dve-1* mutants (right) at the times indicated. Two-tailed Fischer's exact test with Bonferroni correction. Scale bar, 5 μm.

(C) Domain structure of DVE-1. SATB-like domain and homeodomains (HD) are indicated. Site of substitution produced by *uf171* missense mutation (red) and region of *tm4803* deletion mutation (blue) and insertion (red) are indicated. Box, predicted protein structure (AlphaFold) and sequence alignment for HD1 (NCBI Conserved Domains).

(D) Fluorescent confocal images of synaptic iAChR clusters in GABAergic DD processes of the dorsal nerve cord at L4 stage. GABA rescue refers to specific expression of wild type *dve-1* cDNA using the *unc-47* promoter. In this and subsequent figures, iAChR refers to

ACR-12::GFP unless otherwise indicated. Images on each line are from different animals. Scale, 5 µm.

(E) Quantification of the number of iAChR clusters per 25 µm of the L4 stage dorsal nerve cord for the genotypes indicated. Each dot represents a single animal and n for each genotype is indicated by numbers in parentheses. Bars indicate mean ± SEM. ****p<0.0001, ***p<0.001, **p<0.01, *p<0.05, one-way ANOVA with Tukey's multiple comparisons test.

Figure 2. Neuronal DVE-1 is required developmentally for removal of juvenile iAChRs

(A) Schematic of *dve-1(syb7515)* [*dve-1::AID::mScarlet*] crossed with reSi7 [*pan-neuronalpr::TIR1::BFP::AID*].

(B) Timelines of auxin treatments for DVE-1 degradation.

(C) Ventral nerve cord (VNC) images of L4 animals showing *DVE-1::AID::mScarlet* (red), *flp-13pr::ACR-12::GFP* (green), and *TIR1::BFP::AID* (blue) either under control conditions (left) or with continuous auxin treatment from hatch (right). White dashed circle indicates DD1 cell body. Blue arrowhead, intestinal cell. Scale bar, 5 µm.

(D) Quantification of panel C, scatterplot of average *DVE-1::AID::mScarlet* fluorescence in DD1 neurons (left) or intestinal cells (right). Each point represents a single animal. Bars indicate mean ± SEM. ****p<0.0001, ns: not significant, two-tailed students t-test.

(E) Quantification of DD neuron iAChR clusters in the L4 stage dorsal nerve cord for control and *dve-1::AID::mScarlet* animals under treatment conditions described in panel B. Each point represents a single animal. Bars indicate mean ± SEM. ,****p<0.0001, ***p<0.001, two-way ANOVA with Tukey's multiple comparison.

(F) Confocal images of ACR-12::GFP clusters in the dorsal nerve cord of L4 stage *dve-1::AID::mScarlet* animals either under control conditions or with continuous auxin treatment. Scale bar, 5 µm.

(G) Top, scatterplot of LEV-10::GFP dorsal/ventral fluorescence intensity ratio measurements per corresponding 25 µm regions of dorsal and ventral nerve cord expressed as dorsal/ventral fluorescence ratio -1. Bars indicate mean ± SEM. ***p<0.001, ns: not significant two-tailed student's t-test. Bottom, confocal images of LEV-10::GFP from the dorsal nerve cord before (pre-remodeling) and after (post-remodeling) the L1/L2 transition. Scale bar, 5 µm. NATF DD LEV-10 indicates tissue-specific labeling of endogenous LEV-10 by split-GFP [36]. Each point represents a single animal.

(H) Top, confocal images of the dorsal and ventral process from L4 stage wild type and *dve-1(uf171)* mutants co-expressing the mCherry::RAB-3 synaptic vesicle (SV) and ACR-12::GFP (iAChR) markers in DD neurons. Scale bar, 5 µm. Bottom, quantification of iAChR clusters (left) and SV puncta (right) in dorsal and ventral processes of L4 stage DD neurons for wild type and *dve-1(uf171)* mutants. Each point represents a single animal. Bars indicate mean ± SEM. ****p<0.0001, ns: not significant, two-way ANOVA with Tukey's multiple comparison test.

Figure 3. Mutation of *dve-1* enhances the stability of cholinergic presynaptic sites

(A) Top, cell surface iAChR clusters in the L4 stage dorsal nerve cord labeled by anti-HA fluorescence (red). Scale bar, 5 µm. Bottom, scatterplot of dorsal receptor clusters per 25 µm. Each point represents a single animal. Bars indicate mean ± SEM. ***p<0.001, two-tailed students t-test.

(B) Top, lingering clusters of juvenile postsynaptic iAChRs in DD neurons (green) and apposed cholinergic synaptic vesicles (SV, *unc-129pr*::mCherry::RAB-3, red) from L4 stage *dve-1* mutant dorsal nerve cord. Yellow dash indicates area of inset (right). Bottom, line scan shows relative fluorescence intensity of iAChR (green) and SV (red) for the same 30 µm region.

(C) Top, lingering clusters of juvenile postsynaptic iAChRs in DD neurons (green) and presynaptic cholinergic active zone (AZ) marker ELKS-1 (red, *unc-129pr*::ELKS-1::mCherry) from L4 stage *dve-1* mutant dorsal nerve cord. Yellow dash indicates area of inset (right). Bottom, line scan shows relative fluorescence intensity of iAChR (green) and AZ (red) for the same 25 µm region.

(D) The percent apposition between postsynaptic iAChR clusters in DD motor neurons and presynaptic cholinergic SVs or AZs (green). As control, each line scan was shifted by 2 µm to assess percent apposed by chance (black). Each point represents a single animal. Bars indicate mean ± SEM. **** $p<0.0001$, *** $p<0.001$, two-tailed student's t-test.

(E) Synaptic connectivity in the juvenile and mature circuit of wild type (left) and *dve-1* mutants (right). DA/B, dorsally projecting cholinergic motor neurons.

(F) Schematic of photoconversion experiments.

(G) Merged red/green image of wild type (top) and *dve-1(uf171)* mutants (bottom) expressing Dendra2::RAB-3 immediately following photoconversion at 14 hours after hatch (left) and 10 hours later (right). Red channel, magenta. Green channel, cyan. Red fluorescence indicating juvenile SV clusters decreases significantly during wild type remodeling but remains in *dve-1* mutants. Scale bar, 5 µm.

(H) Scatterplot showing red (left) and green (right) Dendra2::RAB-3 fluorescence intensity 10 hours following photoconversion normalized to the fluorescence intensity immediately after photoconversion at 14 hours after hatch (before remodeling) for wild type (left) and *dve-1(uf171)* mutants (right). Each point indicates a single animal. Bars indicate mean ± SEM. ** $p<0.01$, two-tailed student's t-test.

(I) Merged red/green image of wild type (top) and *dve-1(uf171)* mutants (bottom) expressing Dendra2::RAB-3 immediately following photoconversion at 24 hours after hatch (left) and 10 hours later (right). Red channel, magenta. Green channel, cyan. Scale bar, 5 µm.

(J) Scatterplot showing red (left) and green (right) Dendra2::RAB-3 fluorescence intensity 10 hours following photoconversion normalized to fluorescence intensity immediately after photoconversion at 24 hours after hatch (after remodeling) for wild type (left) and *dve-1(uf171)* mutants (right). Each point indicates a single animal. Bars indicate mean ± SEM. **p<0.01, ns: not significant, two-tailed student's t-test.

(K) Left, scatterplot of cholinergic SNB-1::GFP fluorescence intensity in L4 stage dorsal nerve cord (DNC) (*acr-5pr*::SNB-1::GFP) for wild type and *dve-1* mutants. Each point indicates a single animal. Bars indicate mean ± SEM. ****p<0.0001, two-tailed student's t-test. Right, stacked images showing cholinergic SNB-1::GFP clusters in L4 stage dorsal nerve cord of wild type and *dve-1(uf171)* mutants. Each line is from a different animal. Scale bar, 5 µm.

(L) Scatterplot of cholinergic SNB-1::GFP fluorescence intensity in L4 stage ventral nerve cord (*acr-5pr*::SNB-1::GFP) for wild type and *dve-1* mutants. Each point represents a single animal. Bars indicate mean ± SEM. ns: not significant, two-tailed student's t-test.

Figure 4. A failure of synapse elimination in *dve-1* mutants produces dorsal turning bias

(A) Scatter plot showing peak calcium response ($\Delta F/F_0$) in DD and VD GABAergic neurons to photostimulation of presynaptic DA and DB cholinergic neurons for wild type and *dve-1(uf171)* mutants. Horizontal bars indicate mean peak $\Delta F/F_0$ ± SEM. Non-responders are included as zero values. ***p<0.001, one-way ANOVA with Tukey's multiple comparison. n=16 animals for each condition. Number of cells quantified: wt DD: 30, *dve-1(uf171)* DD: 27, wt VD: 64, *dve-1(uf171)* VD: 47.

(B) Representative locomotion tracks for wild type (black) and *dve-1(uf171)* (orange) animals recorded over 5 minutes of single worm tracking on NGM OP50 plates. Scale bar, 1 mm.

(C) Percentage of straight, curved, or circling tracks for wild type and *dve-1(uf171)* mutants. ****p<0.0001, two-tailed Chi-square test. wt: n=14, *dve-1(uf171)* n=15.

(D) Tracks for wild type (left) and *dve-1* mutant (right) animals during forward runs (30 s) prior to or during photostimulation. Asterisks indicate start of track. D/V indicate dorsal and ventral directions.

(E) Schematics of bending angle measurements. Solid orange circles indicate the vertices (head, midbody, and tail) of the body bending angle (blue) measured.

(F) Frequency distribution of body bending angles measured prior to photosimulation for wild type (black) and *dve-1(uf171)* (blue). Negative bending angle values indicate dorsal, while positive bending angle values indicate ventral. Inset highlights bending events greater than 50°. wild type n=17, *dve-1(uf171)* n=13.

(G) Frequency distribution of body bending angles measured during photostimulation for wild type (black) and *dve-1(uf171)* (blue). Negative bending angle values indicate dorsal, while positive bending angle values indicate ventral. Inset highlights bending events greater than 50°. wild type n=17, *dve-1(uf171)* n=13.

(H) Left, scatterplot of total number of dorsal bends greater than 50° before and after photostimulation. Points with connecting lines represent a single animal. Right, average number of dorsal bends greater than 50° during the period of photostimulation for wild type and *dve-1(uf171)* animals. Bars indicate mean ± SEM. ***p*<0.01, two-tailed student's t-test. wild type n=17, *dve-1(uf171)* n=13.

Figure 5. DVE-1-regulated pathways for synapse destabilization act in parallel to *oig-1* antagonism of remodeling

(A) Left, average *oig-1pr::gfp* fluorescence intensity in DD soma of L1 stage wild type and *dve-1* mutants. Each point represents a single DD cell body. Imaged 2 DD neurons/animal. Wild type n=8, *dve-1* mutants n=10. Right, average nuclear DVE-1::GFP fluorescence intensity in DD neurons of L1 stage wild type and *oig-1(ok1687)* mutants. Each point represents a single animal. Bars indicate mean ± SEM. ns: not significant, two-tailed student's t-test.

(B) The percentage of animals where dorsal iAChRs are eliminated for L4 stage wild type, *oig-1(ok1687)*, *dve-1(uf171)* and *dve-1(uf171);oig-1(ok1687)* double mutants. ****p<0.0001, two-tailed Fischer's exact test with Bonferroni Correction.

(C) Left, quantification of average number of iAChR clusters in L4 stage DD neurons per 25 µm of the dorsal nerve cord for the genotypes indicated. Each dot represents a single animal. Bars indicate mean ± SEM. ****p<0.0001, ns: not significant, one-way ANOVA with Tukey's multiple comparisons test. Right, fluorescent confocal images of iAChR clusters in L4 stage DD neurons of the dorsal nerve cord for the genotypes indicated. Scale bar, 5 µm.

(D) The percentage of animals where iAChRs are localized to the ventral side at 10 hours post hatch for wild type, *dve-1(uf171)*, *oig-1(ok1687)* and *dve-1(uf171);oig-1(ok1687)* double mutants. ****p<0.0001, two-tailed Fischer's exact test with Bonferroni Correction.

(E) Left, quantification of average number of iAChR clusters in DD neurons per 25 µm of the ventral nerve cord at L1 stage for the genotypes indicated. Each dot represents a single animal. Bars indicate mean ± SEM. ****p<0.0001, ***p<0.001, ns: not significant, one-way ANOVA with Tukey's multiple comparisons test. Right, fluorescent confocal images of iAChR clusters in the ventral processes of L1 stage DD neurons. Scale bar, 5 µm.

(F) Timeline of development, approximate timing of transitions between larval stages and to adulthood are indicated. Bars indicate the presence of juvenile dorsal iAChRs (top) or ventral iAChRs formed during remodeling (bottom). wild type (grey), *dve-1* mutants (purple), *oig-1* mutants (pink), *oig-1;dve-1* double mutants (green).

Figure 6. The deSUMOylating peptidase ULP-4 regulates DVE-1 nuclear localization

(A) Fluorescence intensity of nuclear DVE-1::GFP in DD motor neurons at 10, 18, 22 and 50 hours after hatch. Nuclear DVE-1::GFP is organized in discrete foci and increases through development. 10 hrs n=10, 18 hrs n=7, 22 hrs n=8, 50 hrs n=9. Each time point indicates mean ± SEM from at least three independent experiments. Inset, representative image of

nuclear DVE-1::GFP in DD motor neuron 18 hours after hatch (nucleus labeled by NLS::mCherry). White dashed line outlines nucleus. Scale bar, 3 μm.

(B) Confocal fluorescence images (left) of DVE-1::GFP in DD GABAergic motor neurons of L1 stage wild type, *ulp-4(lf)* mutant, and *K327R;ulp-4(lf)* double mutants. *ulp-4(lf)* disrupts DVE-1::GFP nuclear localization. White dashed line outlines nucleus. Scale bar, 3 μm. Right, line scan of nuclear DVE-1::GFP fluorescence intensity in DD motor neurons of wild type (green) n=16, *ulp-4(lf)* (blue) n=11 and DVE-1(K327R)*;ulp-4(lf)* double mutants (yellow) n=8. Solid line represents mean, shading represents standard deviation of fluorescence.

(C) Scatterplot (left) of the peak nuclear DVE-1::GFP fluorescence intensity in DD motor neurons. Each point represents a single DD nucleus. Imaged at least 2 DD cells per animal at L1 stage. Wild type: n=16, *ulp-4(lf)*: n=11, *K327R;ulp-4(lf)*: n=8. Bars indicate mean ± SEM. ****p<0.0001, one-way ANOVA with Tukeys multiple comparisons test.

(D) Fluorescent confocal images of iAChR clusters in the dorsal processes of L4 stage DD neurons for genotypes indicated. Scale bar, 5 μm.

(E) Quantification of iAChR clustering at L4 stage for the genotypes indicated. Bars indicate the percentage of L4 stage animals where dorsal iAChRs have been completely removed. ****p<0.0001, *p<0.05, ns: not significant, two-tailed Fischer's exact test with Bonferroni correction. 1/2 pan-neuronal lines, 2/2 GABA lines, and 0/2 intestinal rescue lines restored proper removal of dorsal iAChRs by L4.

(F) Scatterplot of average iAChR fluorescence intensity per 25 μm in the dorsal nerve cord at L4 stage for the genotypes indicated. Each point represents a single animal. Bars indicate mean ± SEM. ****p<0.0001, ***p<0.001, **p<0.01, one-way ANOVA with Tukey's multiple comparisons test.

Figure 7. Disruption of the ubiquitin-proteasome system delays synapse elimination

(A) WormEnrichR pathway analysis using WikiPathway. Bars represent enriched pathways with a combined score >5 (dashed line) and p-adj<0.05.

(B) Activation or inhibition of mtUPR has no effect on synapse elimination. Left, iAChR clusters in the dorsal processes of DD neurons at L4 stage. Scale bar, 5 μm. Right, bars indicate the percentage of L4 stage animals with dorsal iAChRs eliminated. ****p< 0.0001, two-tailed Fischer's exact test, Bonferroni correction.

(C) Top, schematic of Bortezomib inhibitor experimental design. Animals were treated with Bortezomib at 10 hours after hatch until imaging at 24 hours after hatch. Bottom, iAChR clusters in the dorsal DD neuron processes at 24 hours after hatch in control or following bortezomib treatment. Scale bar, 5 μm.

(D) The percentage of animals where dorsal iAChRs are removed by 24 hours after hatch in control or following bortezomib treatment. ****p< 0.0001, two-tailed Fischer's exact test, Bonferroni correction.

(E) Top, schematic of the experimental design for temperature shift experiments. Wild type and *uba-1(it129)* mutants were either maintained at the permissive temperature (15°C) or moved to the restrictive temperature (25ºC) at 10 hrs after hatch before imaging at 30 hours after hatch. Bottom, iAChR clusters in the DD dorsal process of wild type (right) and *uba-1(it129)* (left) mutant animals shifted to restrictive temperature and imaged at 30 hours after hatch. Each line represents the dorsal process of a different animal. Scale bar, 5 μm.

(F) The average fluorescence intensity per 25 μm of wild type or *uba-1(it129)* mutant dorsal nerve cord at the temperature indicated. Bars indicate mean ± SEM. ****p<0.0001, ***p<0.001, ns: not significant, one-way ANOVA with Tukey's multiple comparisons test. Each point represents a single animal.

(G) Schematic for control of remodeling. The transcription factor UNC-30/Pitx regulates the expression of *dve-1* and *oig-1* [23, 24], this paper. *oig-1* encodes an Ig-domain protein that stabilizes juvenile synapses prior to remodeling. Temporal control of *oig-1* expression occurs

through LIN-14- and IRX-1-mediated transcriptional regulation [23, 24]. DVE-1 promotes synapse removal/destabilization, perhaps through UPS transcriptional regulation. Mutation of *dve-1* impairs synapse removal even when OIG-1 mediated stabilization is disrupted.

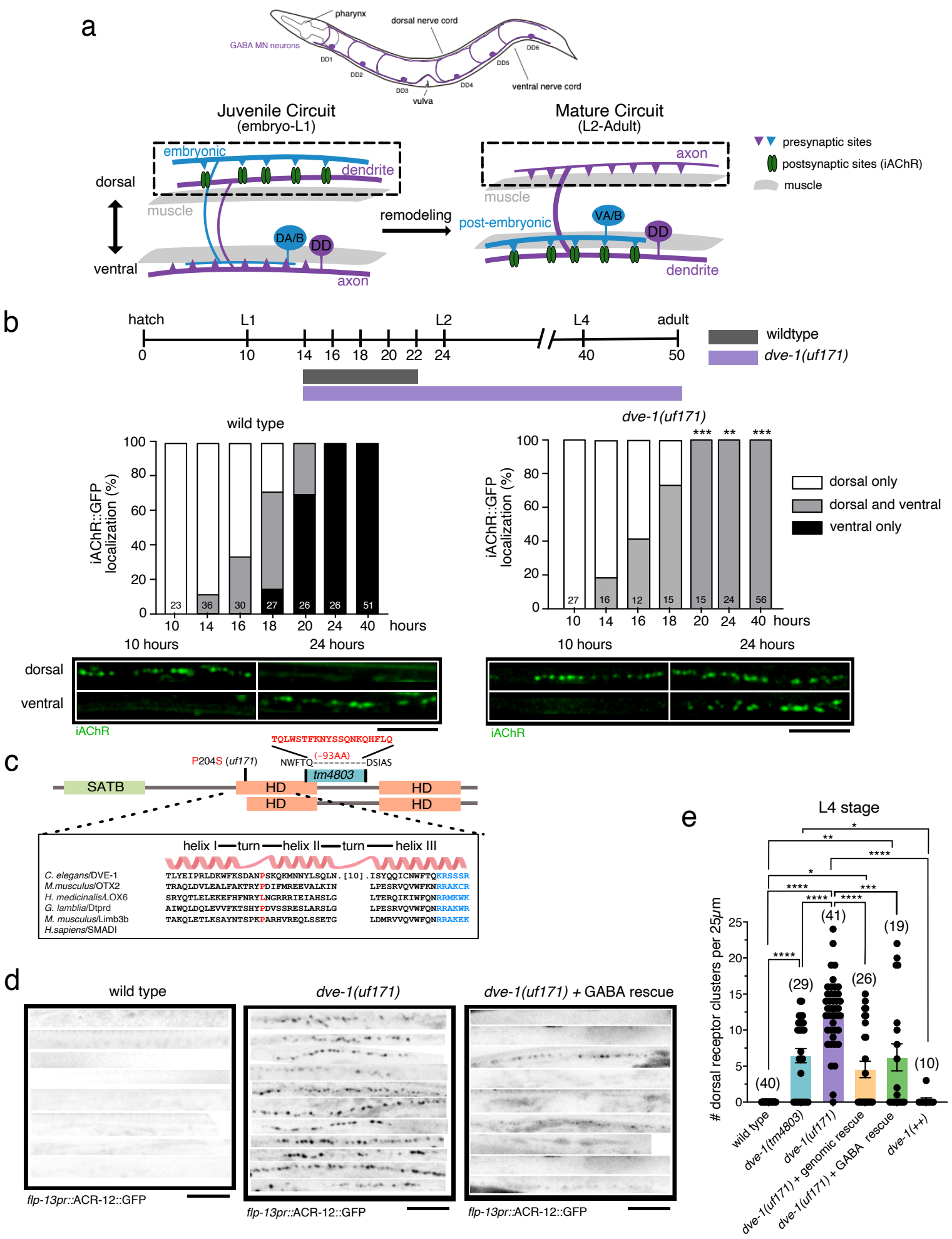
a
pharynx
dorsal nerve cord
GABA MN neurons
DD1
DD2
DD3
DD4
DD5
DD6
vulva
ventral nerve cord
Juvenile Circuit
(embryo-L1)
Mature Circuit
(L2-Adult)
presynaptic sites
postsynaptic sites (iAChR)
muscle
dorsal
ventral
embryonic
dendrite
muscle
DA/B
DD
axon
remodeling
post-embryonic
axon
muscle
VA/B
DD
dendrite
b
hatch
L1
L2
L4
adult
0
10
14
16
18
20
22
24
40
50
wildtype
dve-1(uf171)
wild type
dve-1(uf171)
iAChR::GFP localization (%)
dorsal only
dorsal and ventral
ventral only
23
36
30
27
26
26
51
27
16
12
15
15
24
56
10 hours
24 hours
hours
dorsal
ventral
iAChR
c
TQLWSTFKNYSSQNKQHFLQ
P204S (uf171)
(-93AA)
NWFTQ----------DSIAS
tm4803
SATB
HD
HD
HD
HD
helix I—turn—helix II—turn—helix III
C. elegans/DVE-1 TLYEIPRLDKWFKSDANPSKQKMNNYLSQLN.[10].ISYQQICNWFTQKRSSSR
M.musculus/OTX2 TRAQLDVLEALFAKTRYPDIFMREEVALKIN LPESRVQVWFKNRRAKCR
H. medicinalis/LOX6 SRYQTLELEKEFHFNRYLNGRRRIEIAHSLG LTERQIKIWFQNRRMKWK
G. lamblia/Dtprd AIWQLDQLEVVFKTSHYPDVSSRESLARSLG LPESRVQVWFQNRRAKWR
M. musculus/Limb3b TAKQLETLKSAYNTSPKPARHVREQLSSETG LDMRVVQVWFQNRRAKEK
H.sapiens/SMADI
d
wild type
dve-1(uf171)
dve-1(uf171) + GABA rescue
flp-13pr::ACR-12::GFP
flp-13pr::ACR-12::GFP
flp-13pr::ACR-12::GFP
e
L4 stage
dorsal receptor clusters per 25μm
(40)
(29)
(41)
(26)
(19)
(10)
wild type
dve-1(tm4803)
dve-1(uf171)
dve-1(uf171) + genomic rescue
dve-1(uf171) + GABA rescue
dve-1(++)

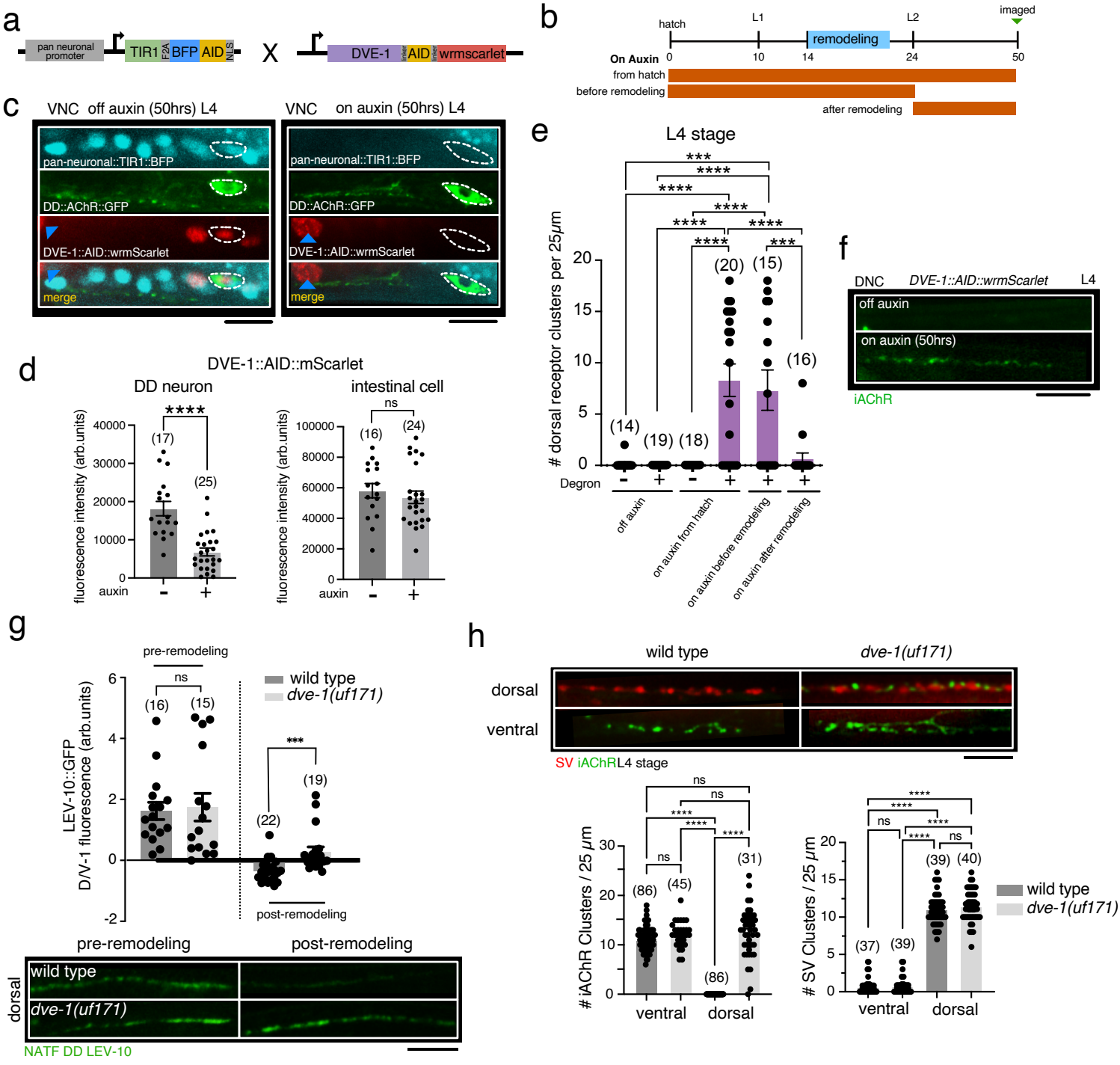
a
pan neuronal promoter
TIR1 F2A BFP AID NLS
X
DVE-1 AID wrmscarlet
b
hatch
L1
L2
imaged
remodeling
On Auxin
0
10
14
24
50
from hatch
before remodeling
after remodeling
c
VNC off auxin (50hrs) L4
VNC on auxin (50hrs) L4
pan-neuronal::TIR1::BFP
DD::AChR::GFP
DVE-1::AID::wrmScarlet
merge
d
DVE-1::AID::mScarlet
DD neuron
intestinal cell
fluorescence intensity (arb.units)
auxin
****
ns
(17)
(25)
(16)
(24)
e
L4 stage
dorsal receptor clusters per 25µm
Degron
off auxin
on auxin from hatch
on auxin before remodeling
on auxin after remodeling
(14)
(19)
(18)
(20)
(15)
(16)
f
DNC
DVE-1::AID::wrmScarlet
L4
off auxin
on auxin (50hrs)
iAChR
g
pre-remodeling
post-remodeling
wild type
dve-1(uf171)
LEV-10::GFP
D/V-1 fluorescence (arb.units)
dorsal
NATF DD LEV-10
h
wild type
dve-1(uf171)
dorsal
ventral
SV iAChRL4 stage
iAChR Clusters / 25 µm
SV Clusters / 25 µm
ventral
dorsal

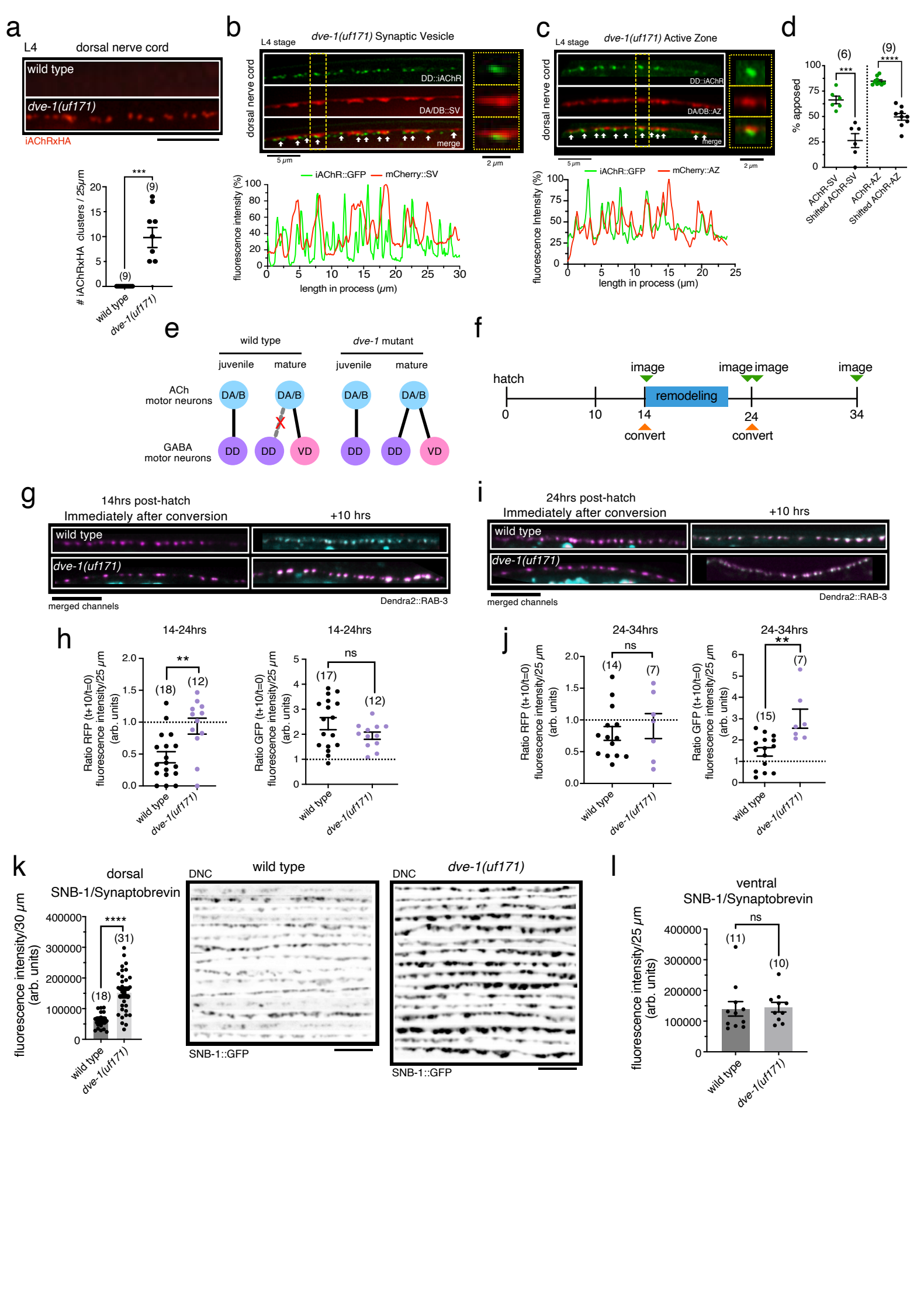
a
L4
dorsal nerve cord
wild type
dve-1(uf171)
iAChRxHA
iAChRxHA clusters / 25µm
***
(9)
wild type
dve-1(uf171)
b
L4 stage
dve-1(uf171) Synaptic Vesicle
dorsal nerve cord
DD::iAChR
DA/DB::SV
merge
5 µm
2 µm
iAChR::GFP
mCherry::SV
fluorescence intensity (%)
length in process (µm)
c
L4 stage
dve-1(uf171) Active Zone
dorsal nerve cord
DD::iAChR
DA/DB::AZ
merge
iAChR::GFP
mCherry::AZ
fluorescence Intensity (%)
length in process (µm)
d
(6)
(9)
***
****
% apposed
AChR-SV
Shifted AChR-SV
AChR-AZ
Shifted AChR-AZ
e
wild type
dve-1 mutant
juvenile
mature
juvenile
mature
ACh motor neurons
GABA motor neurons
DA/B
DD
VD
f
hatch
image
image image
image
remodeling
0
10
14
24
34
convert
convert
g
14hrs post-hatch
Immediately after conversion
+10 hrs
wild type
dve-1(uf171)
merged channels
Dendra2::RAB-3
i
24hrs post-hatch
Immediately after conversion
+10 hrs
wild type
dve-1(uf171)
merged channels
Dendra2::RAB-3
h
14-24hrs
Ratio RFP (t+10/t=0) fluorescence intensity/25 µm (arb. units)
**
(18)
(12)
wild type
dve-1(uf171)
14-24hrs
Ratio GFP (t+10/t=0) fluorescence intensity/25 µm (arb. units)
ns
(17)
(12)
wild type
dve-1(uf171)
j
24-34hrs
Ratio RFP (t+10/t=0) fluorescence intensity/25 µm (arb. units)
ns
(14)
(7)
wild type
dve-1(uf171)
24-34hrs
Ratio GFP (t+10/t=0) fluorescence intensity/25 µm (arb. units)
**
(7)
(15)
wild type
dve-1(uf171)
k
dorsal
SNB-1/Synaptobrevin
fluorescence intensity/30 µm (arb. units)
****
(31)
(18)
wild type
dve-1(uf171)
DNC
wild type
SNB-1::GFP
DNC
dve-1(uf171)
SNB-1::GFP
l
ventral
SNB-1/Synaptobrevin
fluorescence intensity/25 µm (arb. units)
ns
(11)
(10)
wild type
dve-1(uf171)

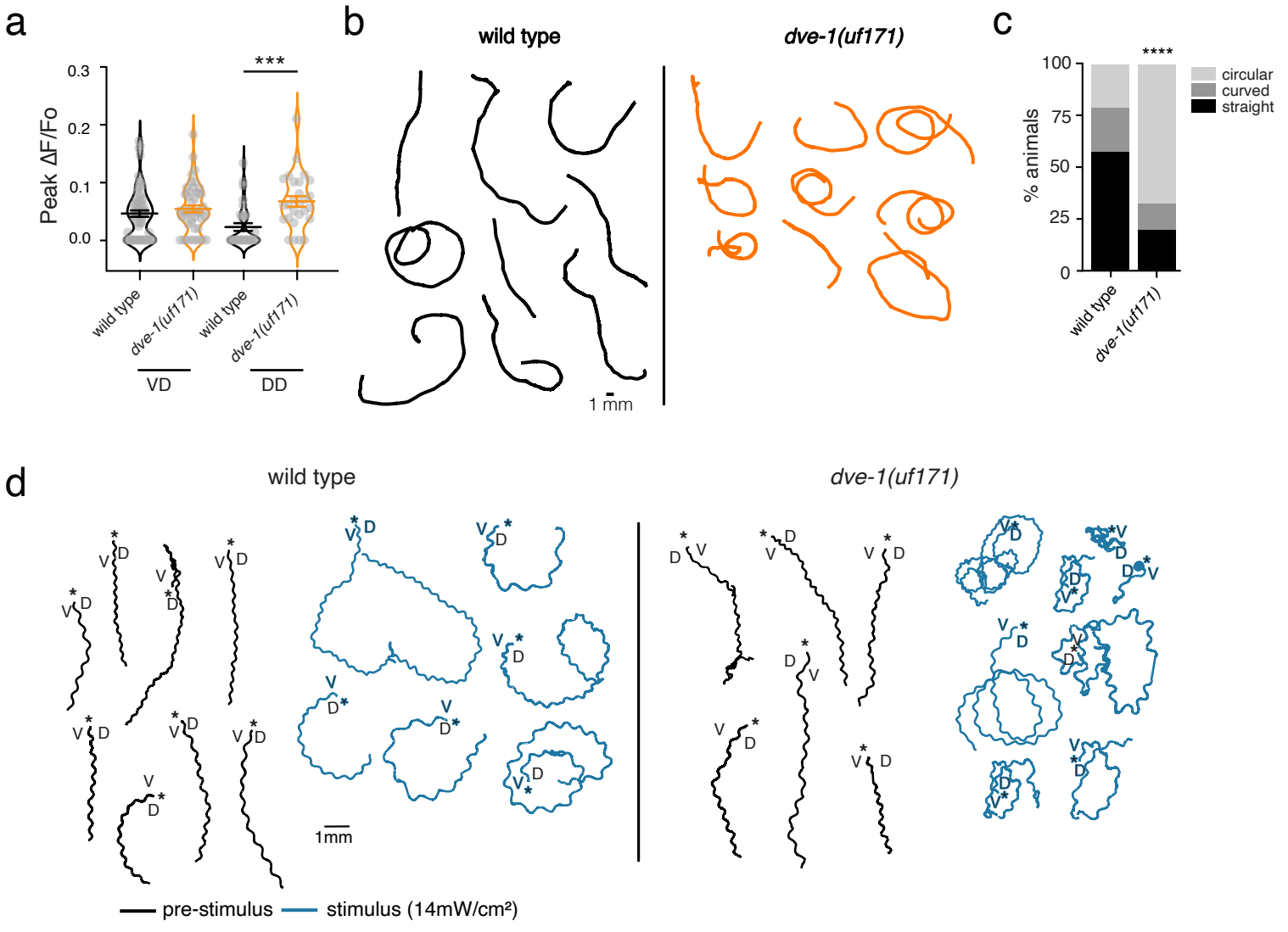
a
Peak ΔF/Fo
0.3
0.2
0.1
0.0
***
wild type
dve-1(uf171)
wild type
dve-1(uf171)
VD
DD
b
wild type
dve-1(uf171)
1 mm
c
% animals
100
75
50
25
0
****
circular
curved
straight
wild type
dve-1(uf171)
d
wild type
dve-1(uf171)
1mm
pre-stimulus
stimulus (14mW/cm²)
e
head
midbody
tail
shallow bend
vulva
tail
- angle
dorsal bend
head
head
+ angle
vulva
tail
ventral bend
f
unstimulated
dorsal
ventral
wild type
dve-1(uf171)
Frequency of bending angles (%)
50
40
30
20
10
0
-150
-100
-50
0
50
100
150
bending angle (degrees)
g
stimulated
dorsal
ventral
wild type
dve-1(uf171)
Frequency of bending angles (%)
bending angle (degrees)
h
Number of dorsal bends >50°
2000
1500
1000
500
0
pre-stimulus
stimulus
pre-stimulus
stimulus
wild type
dve-1(uf171)
n=17
n=13
Average number of dorsal bends >50°
**
(13)
(17)
wild type
dve-1(uf171)

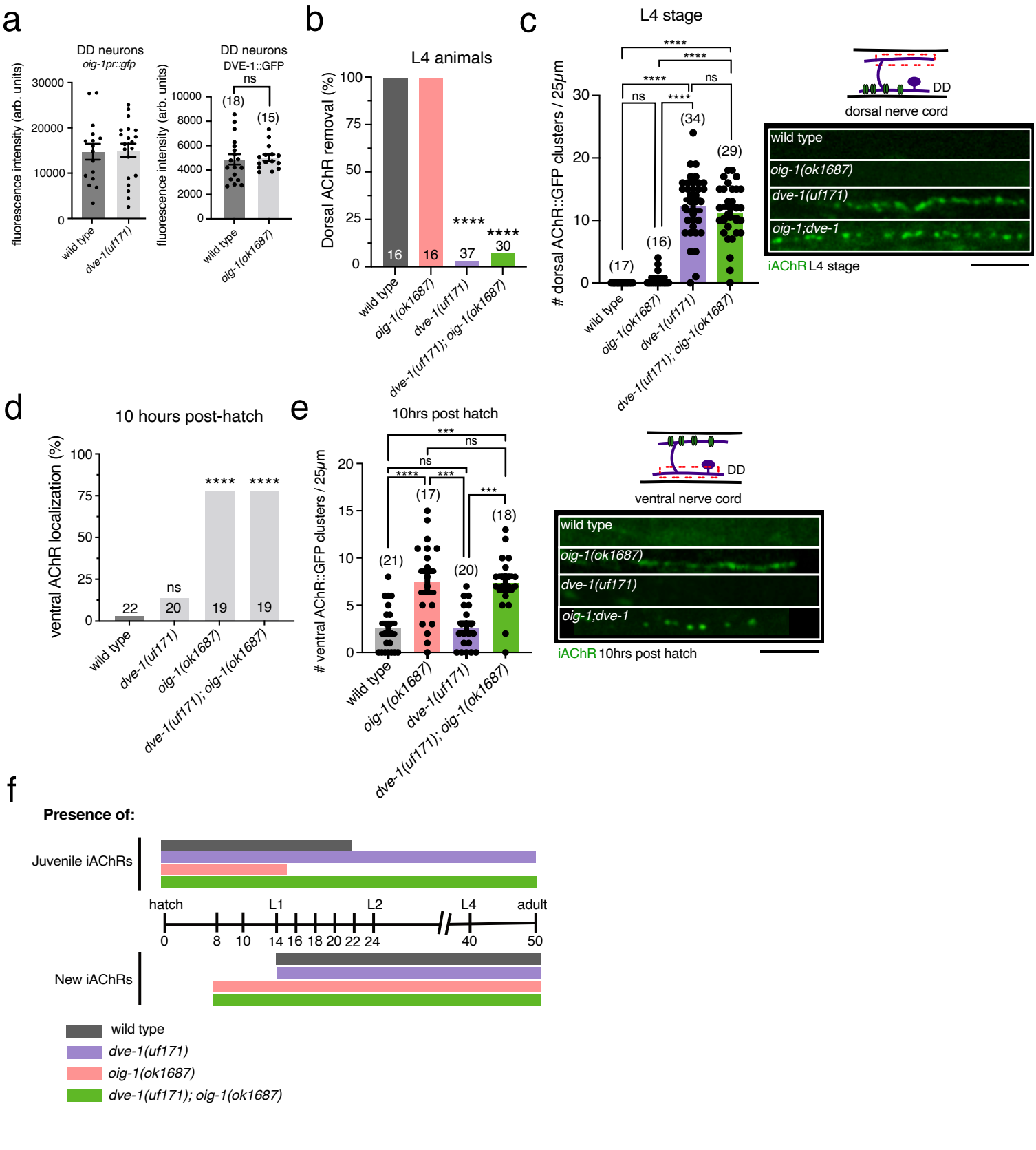
a
DD neurons
oig-1pr::gfp
fluorescence intensity (arb. units)
wild type
dve-1(uf171)
DD neurons
DVE-1::GFP
ns
(18)
(15)
wild type
oig-1(ok1687)
b
L4 animals
Dorsal AChR removal (%)
16
16
37
30
****
wild type
oig-1(ok1687)
dve-1(uf171)
dve-1(uf171); oig-1(ok1687)
c
L4 stage
dorsal AChR::GFP clusters / 25µm
ns
****
(17)
(16)
(34)
(29)
DD
dorsal nerve cord
wild type
oig-1(ok1687)
dve-1(uf171)
oig-1;dve-1
iAChR L4 stage
d
10 hours post-hatch
ventral AChR localization (%)
22
20
19
19
ns
****
e
10hrs post hatch
ventral AChR::GFP clusters / 25µm
(21)
(17)
(20)
(18)
***
ventral nerve cord
iAChR 10hrs post hatch
f
Presence of:
Juvenile iAChRs
hatch
L1
L2
L4
adult
0
8
10
14 16 18 20 22 24
40
50
New iAChRs
wild type
dve-1(uf171)
oig-1(ok1687)
dve-1(uf171); oig-1(ok1687)

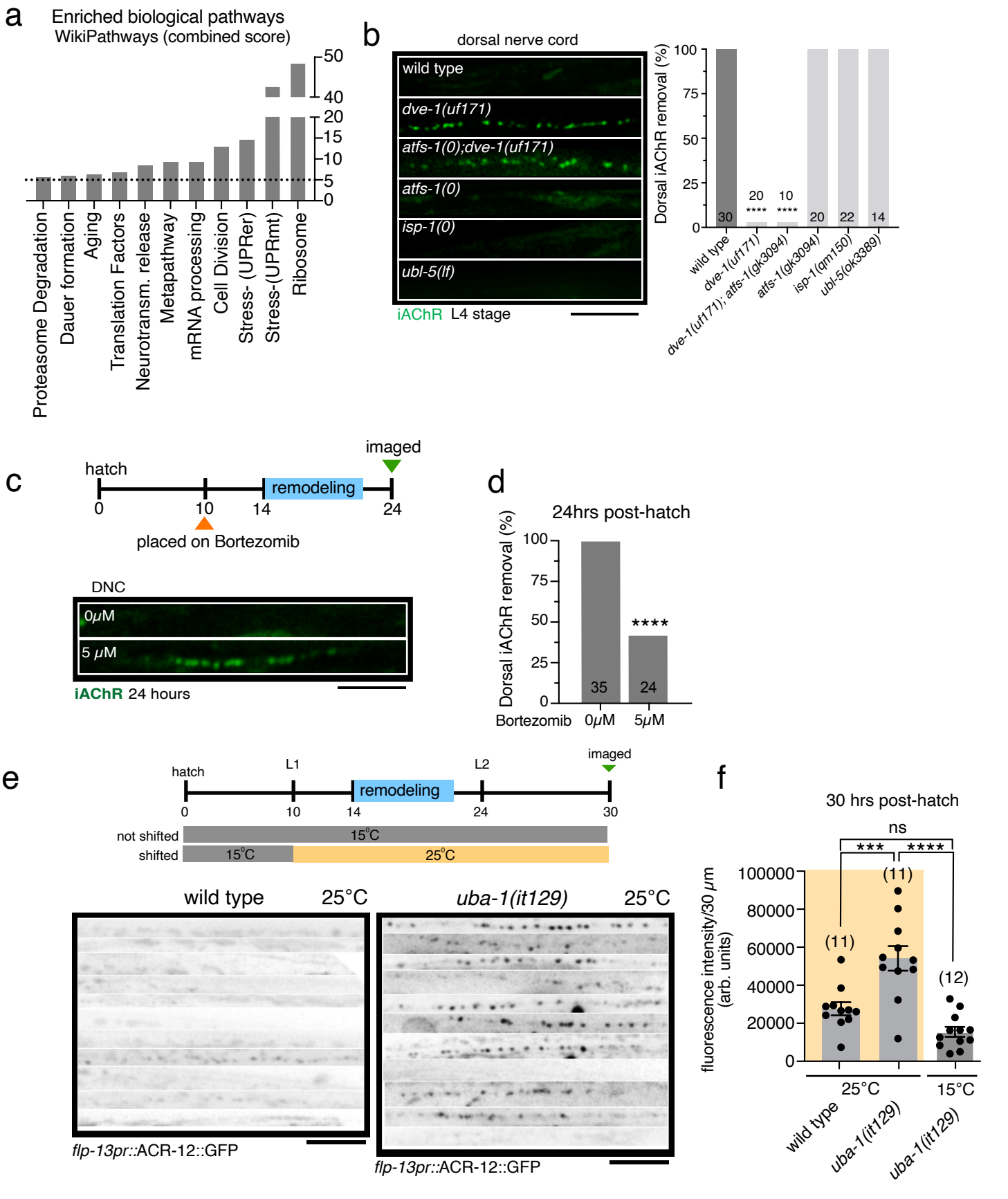
a
Enriched biological pathways
WikiPathways (combined score)
50
40
20
15
10
5
0
Proteasome Degradation
Dauer formation
Aging
Translation Factors
Neurotransm. release
Metapathway
mRNA processing
Cell Division
Stress- (UPRer)
Stress-(UPRmt)
Ribosome
b
dorsal nerve cord
wild type
dve-1(uf171)
atfs-1(0);dve-1(uf171)
atfs-1(0)
isp-1(0)
ubl-5(lf)
iAChR L4 stage
Dorsal iAChR removal (%)
100
75
50
25
0
30
20
****
10
****
20
22
14
wild type
dve-1(uf171)
dve-1(uf171); atfs-1(gk3094)
atfs-1(gk3094)
isp-1(qm150)
ubl-5(ok3389)
c
hatch
imaged
remodeling
0
10
14
24
placed on Bortezomib
DNC
0μM
5 μM
iAChR 24 hours
d
24hrs post-hatch
Dorsal iAChR removal (%)
100
75
50
25
0
****
35
24
Bortezomib
0μM
5μM
e
hatch
L1
L2
imaged
remodeling
0
10
14
24
30
not shifted
15°C
shifted
15°C
25°C
wild type
25°C
uba-1(it129)
25°C
flp-13pr::ACR-12::GFP
flp-13pr::ACR-12::GFP
f
30 hrs post-hatch
ns
***
****
fluorescence intensity/30 μm
(arb. units)
100000
80000
60000
40000
20000
0
(11)
(11)
(12)
25°C
15°C
wild type
uba-1(it129)
uba-1(it129)
g
UNC-30
DVE-1
IRX-1
LIN-14
UPS
other pro-elimination genes
OIG-1
synapse removal
synapse maintenance

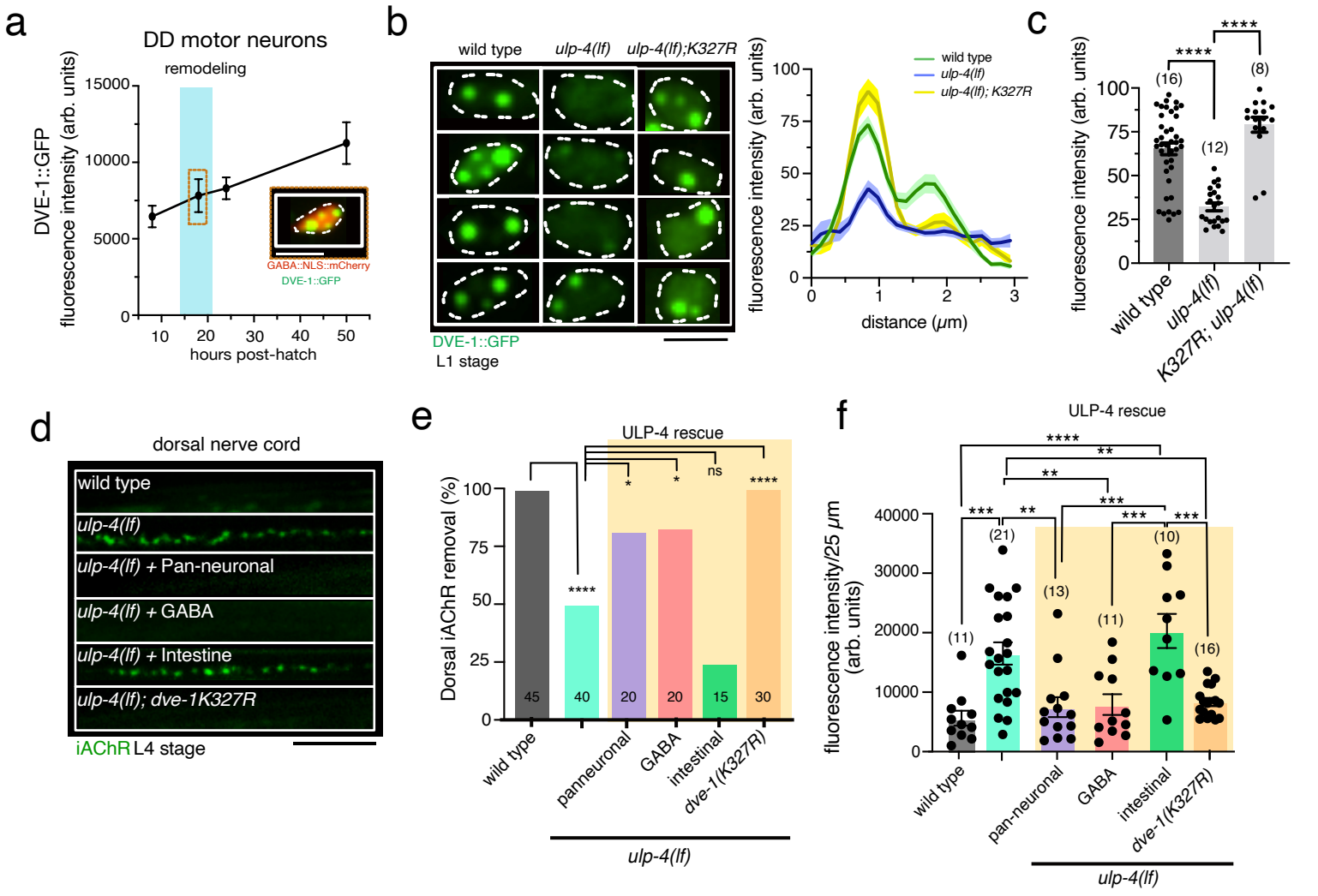
a
DD motor neurons
remodeling
DVE-1::GFP fluorescence intensity (arb. units)
hours post-hatch
GABA::NLS::mCherry
DVE-1::GFP
b
wild type
ulp-4(lf)
ulp-4(lf);K327R
DVE-1::GFP
L1 stage
fluorescence intensity (arb. units)
distance (μm)
c
fluorescence intensity (arb. units)
wild type
ulp-4(lf)
K327R; ulp-4(lf)
d
dorsal nerve cord
wild type
ulp-4(lf)
ulp-4(lf) + Pan-neuronal
ulp-4(lf) + GABA
ulp-4(lf) + Intestine
ulp-4(lf); dve-1K327R
iAChR L4 stage
e
ULP-4 rescue
Dorsal iAChR removal (%)
wild type
panneuronal
GABA
intestinal
dve-1(K327R)
ulp-4(lf)
f
ULP-4 rescue
fluorescence intensity/25 μm (arb. units)
wild type
pan-neuronal
GABA
intestinal
dve-1(K327R)
ulp-4(lf)

Supplemental Figures

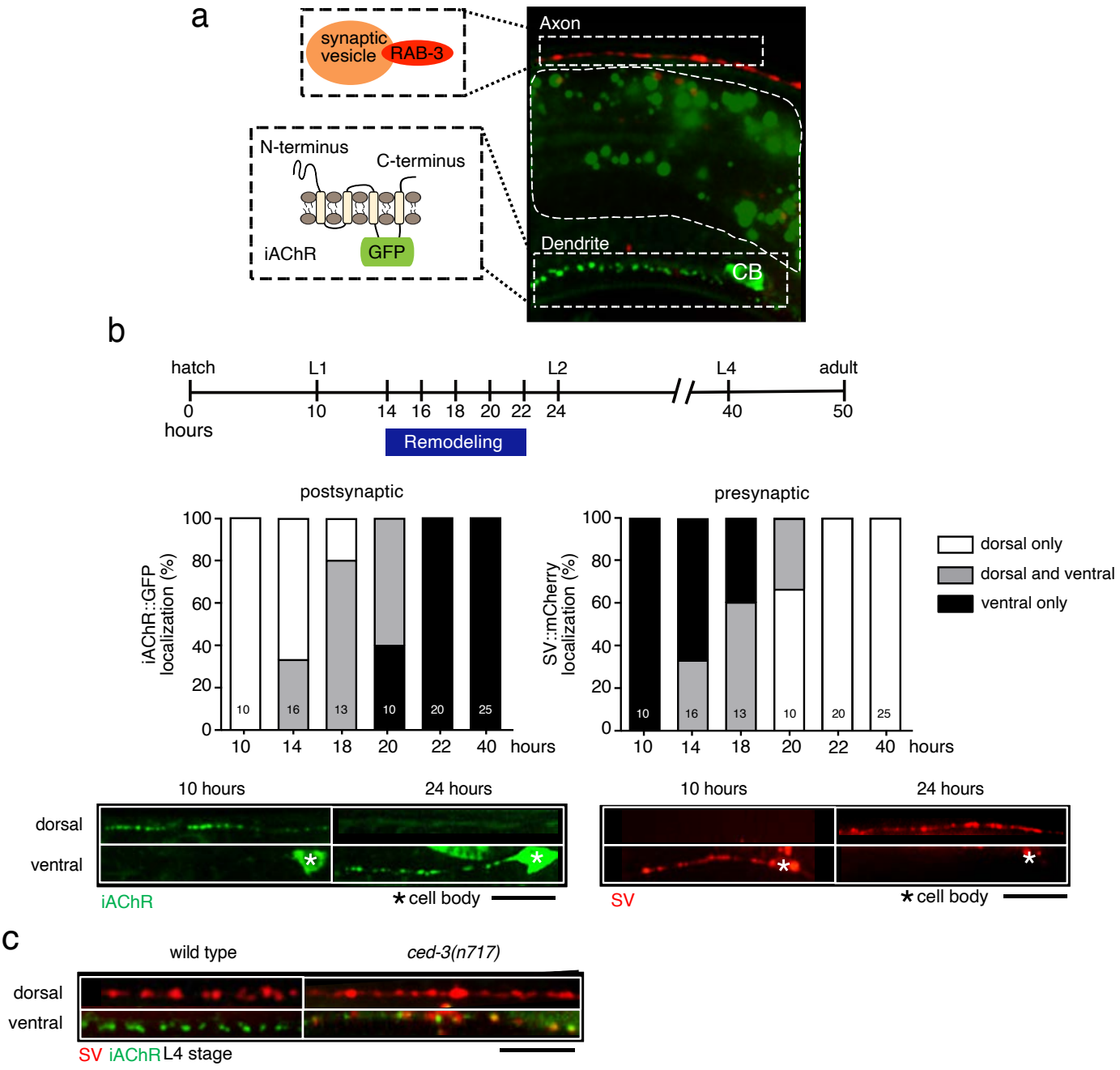

Supplemental Figure 1.1. Remodeling of cholinergic postsynaptic sites and GABAergic presynaptic terminals occur simultaneously but are regulated through different mechanisms

(A) Schematics and confocal image of L4 stage wild type animal co-expressing the synaptic vesicle marker mCherry::RAB-3 with the iAChR marker ACR-12::GFP in DD neurons. Insets are schematics of each marker. Masking of intestinal autofluorescence is outlined by white dotted line.

(B) Top, timeline of wild type development. Approximate timing of transitions between larval stages and to adulthood are indicated. Blue bar indicates duration of DD synaptic remodeling in wild type animals. Middle, quantification of iAChR (postsynaptic) remodeling (left) and SV (presynaptic) remodeling in DD neurons (right) at the indicated time points after hatch. Animals are binned as dorsal only (white), ventral only (black), or dorsal and ventral (grey) according to the distribution of iAChR (left) or SV (right) clusters. Bottom, representative images of dorsal and ventral iAChR clusters (left) and SV puncta (right) at the times indicated in DD neurons of wild type animals. Remodeling of iAChR clusters and SV puncta occur simultaneously. Scale bar, 5 μm.

(C) Merged confocal images showing SV puncta (red) and iAChR clusters (green) in dorsal and ventral DD neuron processes of L4 stage wild type (left) and *ced-3(n717)* mutants (right). Scale bar, 5 μm.

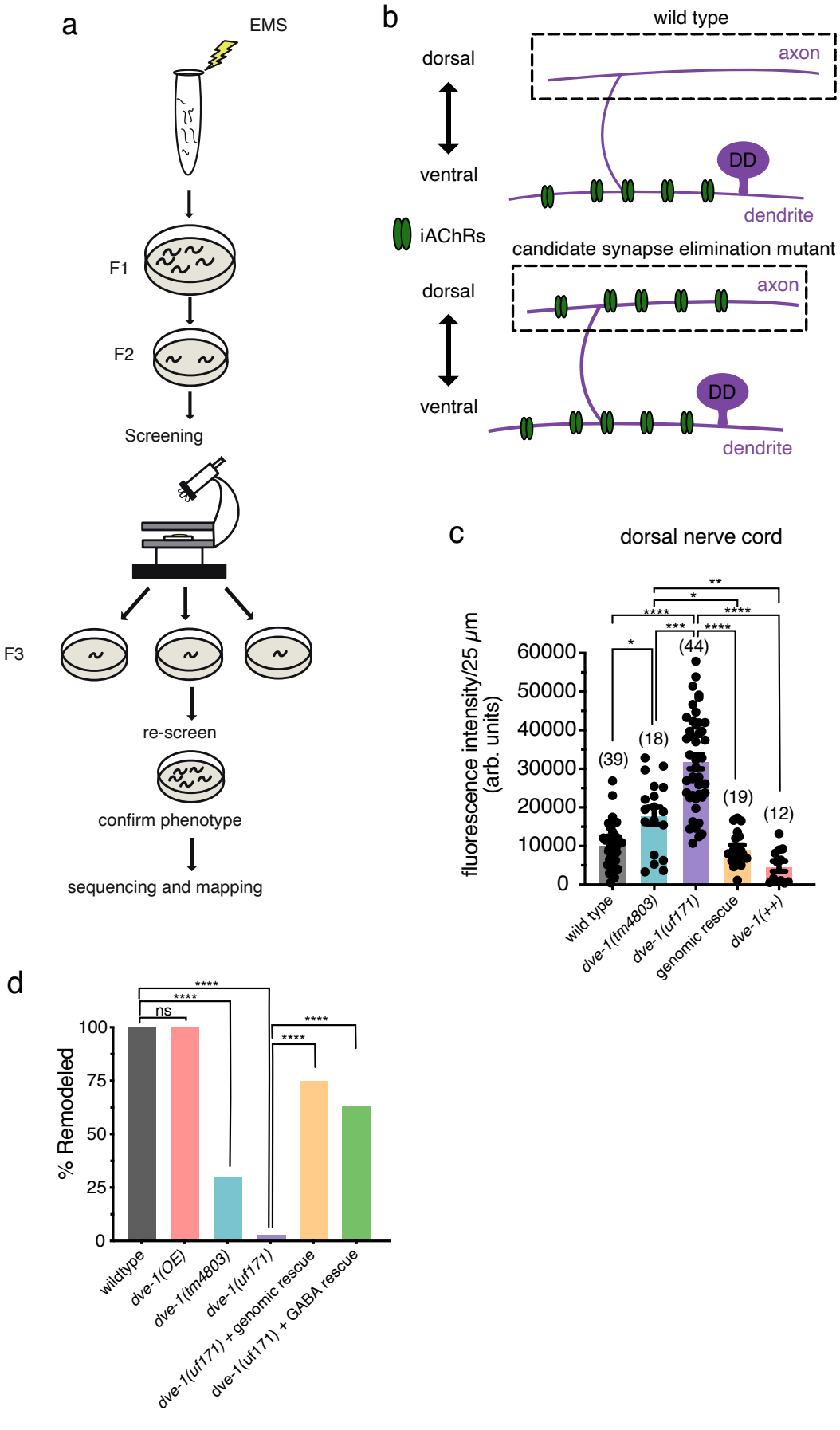
a
EMS
F1
F2
Screening
F3
re-screen
confirm phenotype
sequencing and mapping
b
wild type
dorsal
ventral
axon
DD
dendrite
iAChRs
candidate synapse elimination mutant
dorsal
ventral
axon
DD
dendrite
c
dorsal nerve cord
fluorescence intensity/25 µm (arb. units)
60000
50000
40000
30000
20000
10000
0
(39)
(18)
(44)
(19)
(12)
wild type
dve-1(tm4803)
dve-1(uf171)
genomic rescue
dve-1(+)
d
% Remodeled
100
75
50
25
0
ns
wildtype
dve-1(OE)
dve-1(tm4803)
dve-1(uf171)
dve-1(uf171) + genomic rescue
dve-1(uf171) + GABA rescue

Supplemental Figure 1.2. A Forward genetic screen to identify conserved mechanisms controlling synapse elimination

(A) Schematic of experimental workflow for ethyl methanesulfonate (EMS) screen to obtain mutants with defects in the elimination of juvenile dorsal iAChR clusters.

(B) Schematics of iAChR localization within DD neurons of L4 stage wild type (left) or potential synapse elimination mutant (right).

(C) Quantification of the average ACR-12::GFP fluorescence intensity per 25 µm in the dorsal nerve cord. Bars indicate mean ± SEM. Only significant comparisons shown, ****p<0.0001, ***p<0.001, **p<0.01, *p<0.05, one-way ANOVA with tukey's multiple comparisons test. Each point represents a single animal.

(D) The percentage of L4 stage animals where dorsal iAChRs have been completely removed. ****p<0.0001, two-tailed Fischer's exact test with Bonferroni Correction. Complete remodeling: ventral AChRs only. Incomplete remodeling: dorsal and ventral AChRs.

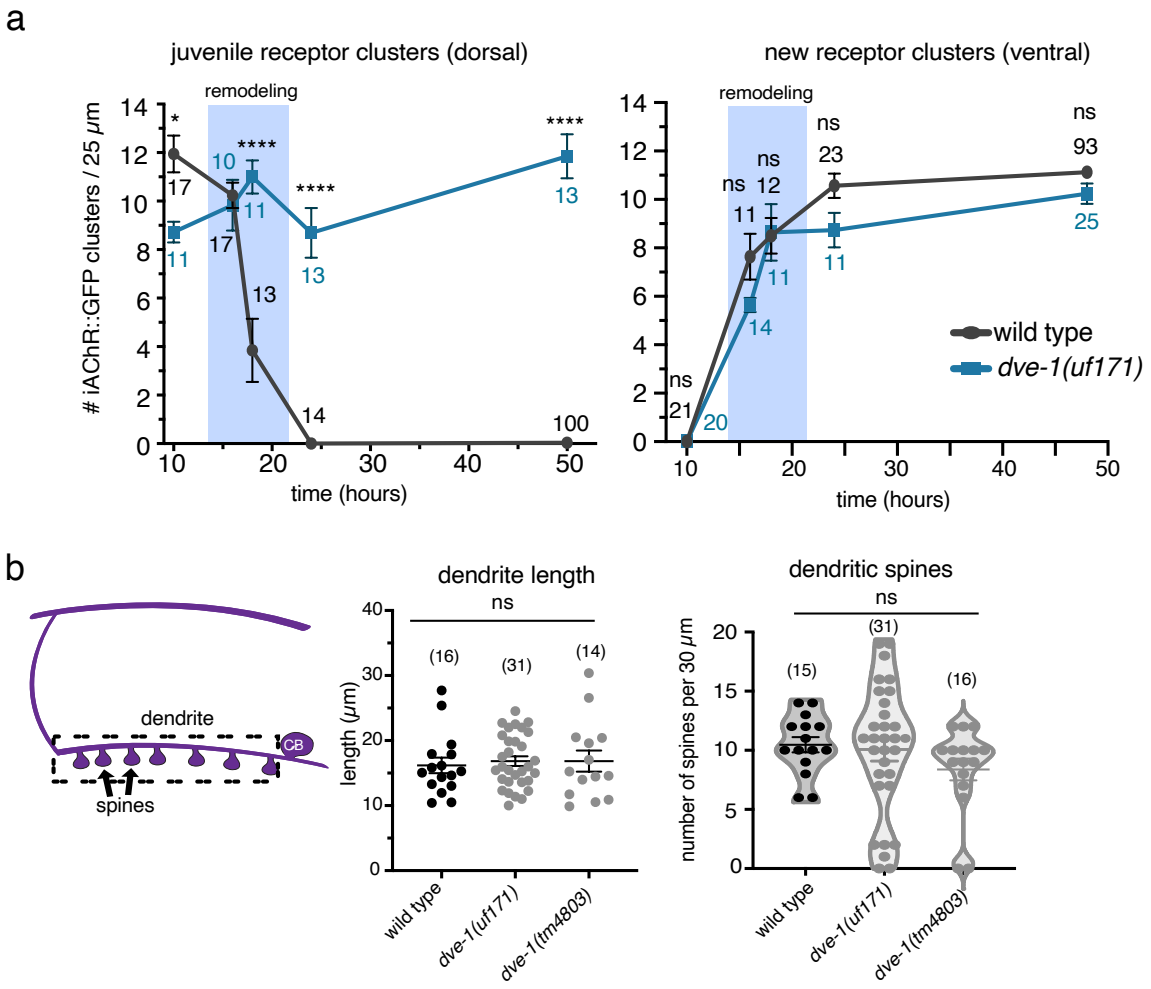
a
juvenile receptor clusters (dorsal)
new receptor clusters (ventral)
remodeling
iAChR::GFP clusters / 25 µm
time (hours)
wild type
dve-1(uf171)
b
dendrite
CB
spines
dendrite length
dendritic spines
length (µm)
number of spines per 30 µm
wild type
dve-1(uf171)
dve-1(tm4803)
c
dve-1(uf171) presynaptic
dorsal only
dorsal and ventral
ventral only
SV::mCherry localization (%)
hours

Supplemental Figure 2.1. *dve-1* mutation disrupts synapse elimination but does not affect new synapse formation

(A) Average number of juvenile iAChR clusters in the dorsal nerve cord (left) and new iAChR clusters in the ventral nerve cord (right) at the indicated times after hatch. iAChR clusters are removed from the dorsal nerve cord of wild type animals (black) during remodeling (blue shading) but persist in in the dorsal nerve cord of *dve-1* mutants (blue). iAChR clusters in the ventral nerve cords of wild type and *dve-1* mutants increase similarly over time. Data points indicate mean ± SEM. ****p<0.0001, two-tailed student's t-test.

(B) Far left: Schematic of DD neuron, segmented box represents area quantified in D. Arrows indicate dendritic spines. CB, cell body. Scatterplots of average length of DD neuron dendrite (left) and number of dendritic spines (right) in wild type, *dve-1(uf171)*, *dve-1(tm4803)* overlayed with a violin plot to show distribution. Each point represents a single animal. Line represents mean ± SEM. ns: not significant.

(C) Quantification of GABA synaptic vesicle (mCherry::RAB-3) remodeling in DD neurons at the indicated time points after hatch in *dve-1(uf171)* mutant animals. Animals are binned as dorsal only (white), ventral only (black), or dorsal and ventral (grey) according to the distribution of SV clusters. See S1.1B for wild type comparison.

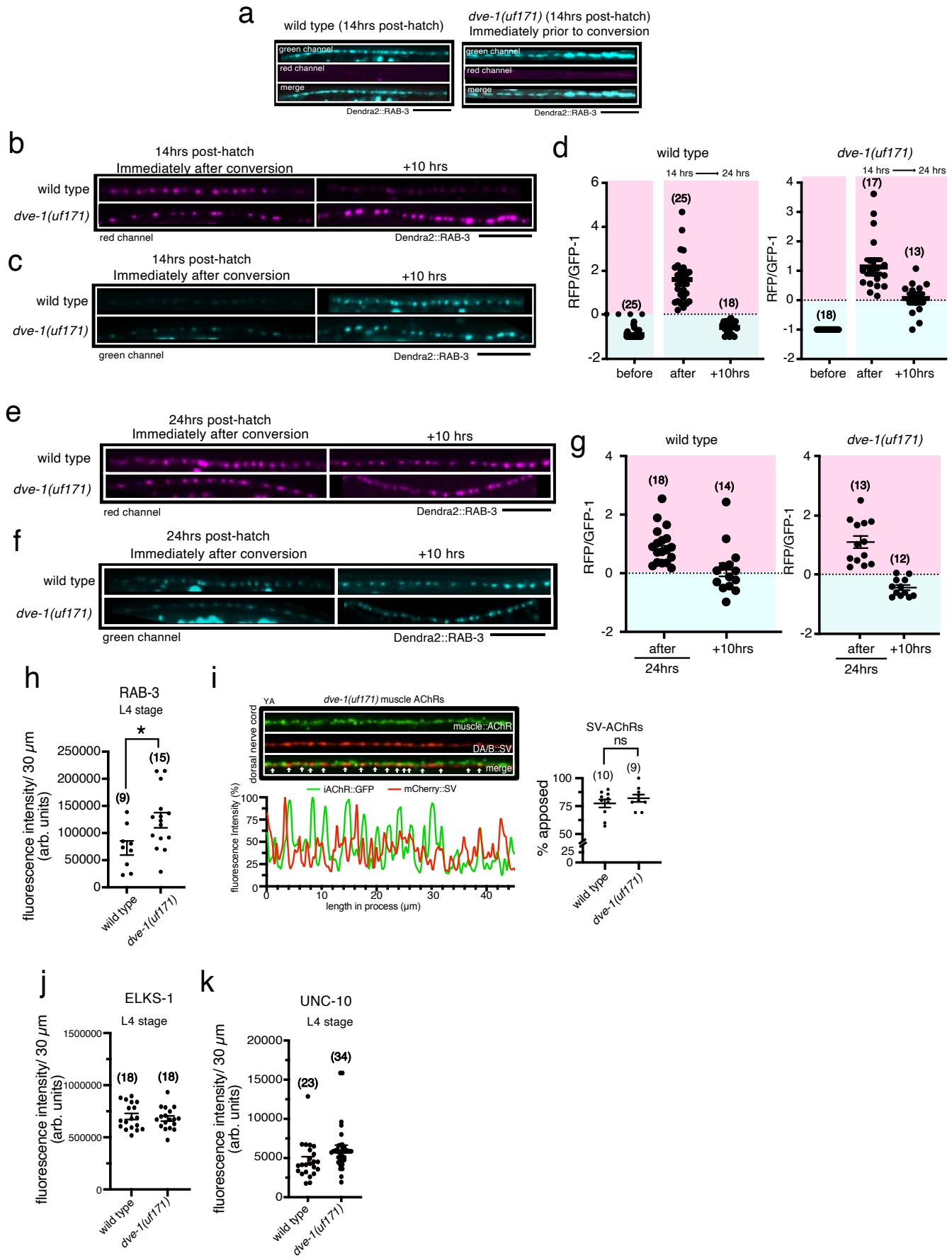
a
wild type (14hrs post-hatch)
dve-1(uf171) (14hrs post-hatch)
Immediately prior to conversion
green channel
red channel
merge
Dendra2::RAB-3
b
14hrs post-hatch
Immediately after conversion
+10 hrs
wild type
dve-1(uf171)
red channel
Dendra2::RAB-3
c
14hrs post-hatch
Immediately after conversion
+10 hrs
wild type
dve-1(uf171)
green channel
Dendra2::RAB-3
d
wild type
dve-1(uf171)
14 hrs ⟶ 24 hrs
RFP/GFP-1
(25)
(18)
(17)
(13)
before
after
+10hrs
e
24hrs post-hatch
Immediately after conversion
+10 hrs
wild type
dve-1(uf171)
red channel
Dendra2::RAB-3
f
24hrs post-hatch
Immediately after conversion
+10 hrs
wild type
dve-1(uf171)
green channel
Dendra2::RAB-3
g
wild type
dve-1(uf171)
RFP/GFP-1
(18)
(14)
(13)
(12)
after
24hrs
+10hrs
h
RAB-3
L4 stage
fluorescence intensity/ 30 µm
(arb. units)
*
(9)
(15)
wild type
dve-1(uf171)
i
YA
dve-1(uf171) muscle AChRs
dorsal nerve cord
muscle::AChR
DA/B::SV
merge
iAChR::GFP
mCherry::SV
fluorescence Intensity (%)
length in process (µm)
SV-AChRs
ns
(10)
(9)
% apposed
wild type
dve-1(uf171)
j
ELKS-1
L4 stage
fluorescence intensity/ 30 µm
(arb. units)
(18)
(18)
wild type
dve-1(uf171)
k
UNC-10
L4 stage
fluorescence intensity/ 30 µm
(arb. units)
(23)
(34)
wild type
dve-1(uf171)

Supplemental Figure 3.1. Presynaptic cholinergic synaptic vesicles turnover during remodeling

(A) Dendra2::RAB-3 clusters in the dorsal nerve cord of wild type (left) and *dve-1(uf171)* mutants (right) prior to photoconversion.

(B) Cholinergic Dendra2::RAB-3 clusters (red channel) in the dorsal nerve cord (*unc-129pr*::Dendra2::RAB-3) of wild type (top) and *dve-1(uf171)* mutants (bottom) either immediately after green to red photoconversion at 14 hours after hatch (left) or 10 hours later (right). Juvenile Dendra2::RAB-3 clusters are largely removed during wild type remodeling but are more stable in *dve-1* mutants. Scale bar, 5 μm.

(C) Cholinergic Dendra2::RAB-3 clusters (green channel) in the dorsal nerve cord of wild type (top) and *dve-1(uf171)* mutants (bottom) either immediately after green to red photoconversion at 14 hours after hatch (left) or 10 hours later (right). Green Dendra2::RAB-3 clusters are similarly added during remodeling of wild type and *dve-1* mutants. Scale bar, 5 μm.

(D) Scatterplots of Dendra2::RAB-3 RFP/GFP fluorescence intensity ratios before photoconversion at 10 hours after hatch (before remodeling), immediately after, and 10 hours later for wild type and *dve-1* mutants. Expressed as RFP/GFP fluorescence ratio -1 for display purposes. Negative values indicate enhanced green fluorescence while positive values enhanced red fluorescence. Each dot represents a single animal.

(E) Cholinergic Dendra2::RAB-3 clusters (red channel) in the dorsal nerve cord of wild type (top) and *dve-1(uf171)* mutants (bottom) either immediately after green to red photoconversion at 24 hours after hatch (left) or 10 hours later (right). For both wild type and *dve-1*, photoconverted cholinergic Dendra2::RAB-3 clusters are stable following remodeling. Scale bar, 5 μm.

(F) Cholinergic Dendra2::RAB-3 clusters (green channel) in the dorsal nerve cord of wild type (top) and *dve-1(uf171)* mutants (bottom) either immediately after green to red photoconversion at 24 hours after hatch (left) or 10 hours later (right). Scale bar, 5 µm.

(G) Scatterplots of Dendra2-RAB-3 RFP/GFP fluorescence intensity ratios before photoconversion at 24 hours after hatch (following remodeling), immediately after, and 10 hours later for wild type and *dve-1* mutants. Expressed as RFP/GFP fluorescence ratio-1 for display purposes. Negative values indicate enhanced green fluorescence while positive values indicate enhanced red fluorescence. Each dot represents a single animal.

(H) Scatterplot of cholinergic mCherry::RAB-3 fluorescence intensity (*unc-129pr*::mCherry::RAB-3) in L4 stage dorsal nerve cord (DNC) for wild type and *dve-1* mutants. Each point indicates a single animal. Bars indicate mean ± SEM. *p<0.01, two-tailed student's t-test.

(I) Top, apposition of dorsal muscle iAChRs (*myo-3pr*::ACR-16::GFP, green) and cholinergic synaptic vesicles (SV, *acr-5pr*::mCherry::RAB-3, red) in the dorsal nerve cord of L4 stage *dve-1* mutant. Bottom, line scan of relative muscle iAChR (green) and cholinergic SV (red) fluorescence intensity for the same 44 µm region. Right, percent apposition between muscle iAChR and cholinergic SV clusters for wild type and *dve-1(uf171*) mutants. Each point represents a single animal. Bars indicate mean ± SEM. ns: not significant, two-tailed student's t-test.

(J) Scatterplot of cholinergic ELKS-1::mCherry fluorescence intensity (*unc-129pr*::ELKS-1::mCherry) in L4 stage dorsal nerve cord (DNC) for wild type and *dve-1* mutants. Each point indicates a single animal. Bars indicate mean ± SEM.

(K) Scatterplot of cholinergic UNC-10::GFP fluorescence intensity (*acr-5pr*::UNC-10::GFP) in L4 stage dorsal nerve cord (DNC) for wild type and *dve-1* mutants. Each point indicates a single animal. Bars indicate mean ± SEM.

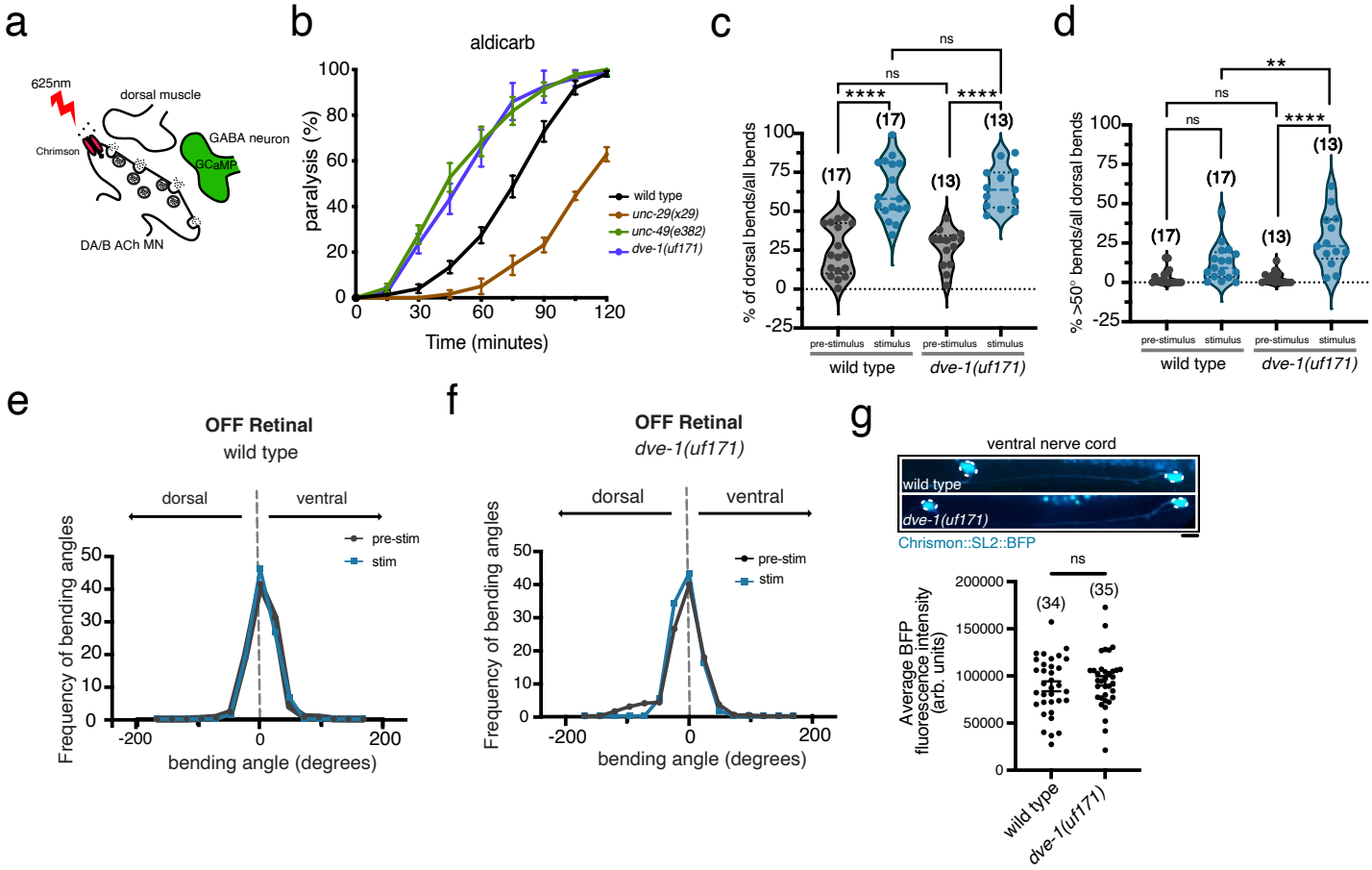
a
625nm
dorsal muscle
Chrimson
GABA neuron
GCaMP
DA/B ACh MN
b
aldicarb
paralysis (%)
Time (minutes)
wild type
unc-29(x29)
unc-49(e382)
dve-1(uf171)
c
% of dorsal bends/all bends
ns
****
(17)
(13)
pre-stimulus
stimulus
wild type
dve-1(uf171)
d
% >50° bends/all dorsal bends
**
ns
****
e
OFF Retinal
wild type
dorsal
ventral
pre-stim
stim
Frequency of bending angles
bending angle (degrees)
f
OFF Retinal
dve-1(uf171)
g
ventral nerve cord
wild type
dve-1(uf171)
Chrismon::SL2::BFP
Average BFP fluorescence intensity (arb. units)
(34)
(35)

Supplemental Figure 4.1. Motor circuit function is disrupted in *dve-1* mutants

(A) Schematic of combined cell-specific expression of Chrimson (red receptor) for cholinergic depolarization, and GCaMP6s monitoring [Ca^{2+}] changes in the post-synaptic GABAergic motor neurons (green).

(B) Time course of paralysis in the presence of aldicarb (1 mM) for wild type (black) (n=14), *unc-29(x29)* mutants (brown) (n=6), *unc-49(e382)* mutants (dark green) (n=16), *dve-1(uf171)* mutants (blue) (n=12), are shown. At least 10 animals per trial. Data represent mean ± SEM.

(C) Scatterplot with violin overlay of the percentage of dorsal bends for wild type and *dve-1(uf171)* mutants before and after photostimulation. Each point represents a single animal. ****p<0.0001, ns: not significant, two way ANOVA with Tukey's multiple comparisons test.

(D) Scatterplot with violin overlay of the percentage of dorsal turns greater than 50° wild type (black) and *dve-1(uf171)* (blue) before and after photostimulation. Each point represents a single animal. ****p<0.0001, **p<0.01, ns - not significant, two way ANOVA with Tukey's multiple comparisons test.

(E) Frequency distribution of body bending angles prior to (black) and during photostimulation (blue) for control animals in the absence of all-trans-retinal. Negative bending angle values indicate dorsal, while positive bending angle values indicate ventral. n=3.

(F) Frequency distribution of body bending angles prior to (black) and during photostimulation (blue) for *dve-1* mutants in the absence of all-trans-retinal. Negative bending angle values indicate dorsal, while positive bending angle values indicate ventral. n=3.

(G) Top, confocal images of DA/DB motor neurons from control and *dve-1(uf171)* mutant animals expressing *punc-129::*Chrimson*::SL2::BFP*. Scale bar, 5 µm. Bottom, average fluorescence intensity of DA/DB neuron cell bodies labeled by *punc-129::*Chrimson*::SL2::BFP*. Each dot represents a single DA/DB cell body, at least 15 animals per genotype were imaged.

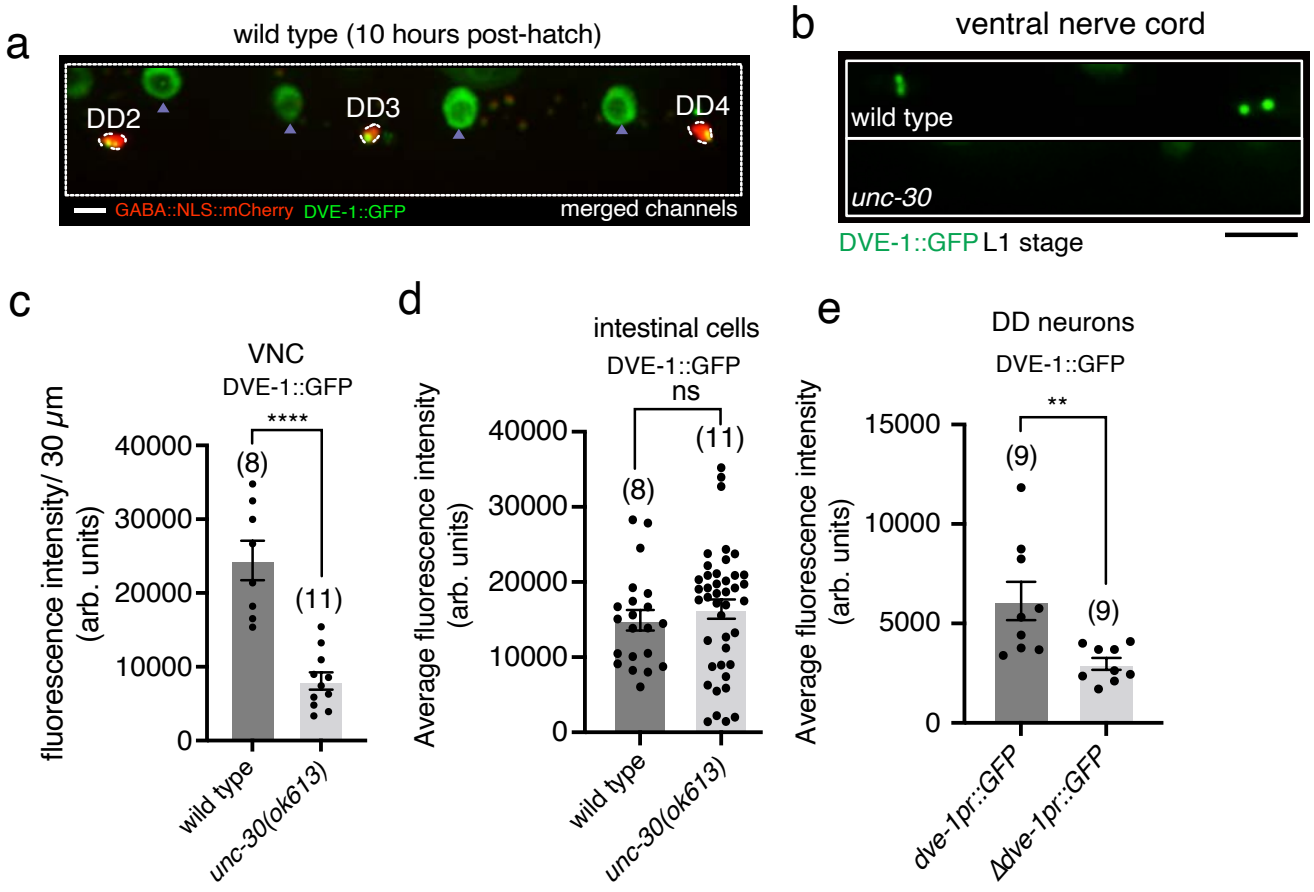
a
wild type (10 hours post-hatch)
DD2
DD3
DD4
GABA::NLS::mCherry DVE-1::GFP
merged channels
b
ventral nerve cord
wild type
unc-30
DVE-1::GFP L1 stage
c
VNC
DVE-1::GFP
fluorescence intensity/ 30 µm (arb. units)
****
(8)
(11)
wild type
unc-30(ok613)
d
intestinal cells
DVE-1::GFP
ns
Average fluorescence intensity (arb. units)
(8)
(11)
wild type
unc-30(ok613)
e
DD neurons
DVE-1::GFP
**
Average fluorescence intensity (arb. units)
(9)
(9)
dve-1pr::GFP
Δdve-1pr::GFP

Supplemental Figure 6.1. The Pitx family transcription factor UNC-30 regulates expression of DVE-1 in GABAergic neurons

(A) Ventral nerve cord expression of DVE-1::GFP in DD GABAergic motor neurons (white outlines) of L1 stage wild type animals. Blue arrowheads indicate intestinal cells. Scale bar, 5 μm.

(B) Images of ventral nerve cord DVE-1::GFP expression in DD GABAergic motor neurons of L1 stage wild type and *unc-30(ok613)* mutants. Scale bar, 5 μm.

(C) Scatterplot of average DVE-1::GFP fluorescence intensity in 30 μm region of ventral nerve cord. Each dot represents a single animal. Bars indicate mean ± SEM. ****$p<0.0001$, two-tailed student's t-test.

(D) Scatterplot of average DVE-1::GFP fluorescence intensity in intestinal cells of L1 stage wild type and *unc-30(ok613)* mutants. Each point represents a single intestinal cell. Imaged 3 intestinal cells per animal. Bars indicate mean ± SEM. ns: not significant, two-tailed student's t-test.

(E) Scatterplot of average nuclear GFP fluorescence intensity in DD neurons of L1 stage animals expressing either DVE-1::GFP using either native ~5 kb *dve-1* promoter region [*dve-1pr::DVE-1::GFP*] or the same promoter region lacking putative UNC-30 binding sites *[*Δ*dve-1pr::DVE-1::GFP*]. Each point represents a single DD1 neuron from a different animal. Bars indicate mean ± SEM. **p<0.001, two-tailed student's t-test.

a

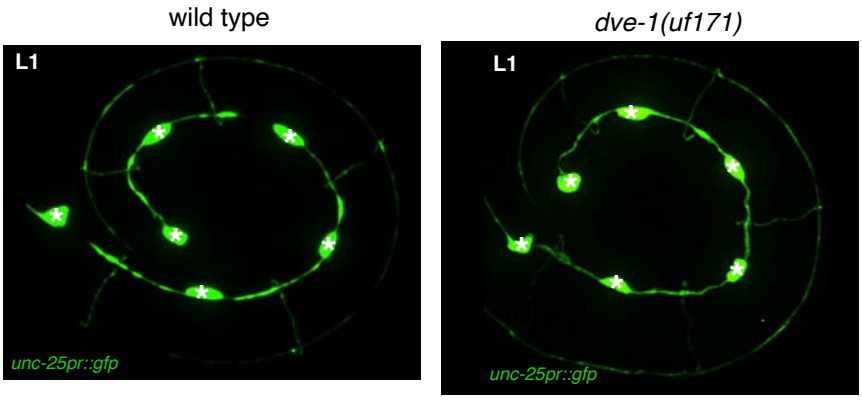
wild type
dve-1(uf171)
L1
L1
unc-25pr::gfp
unc-25pr::gfp

b

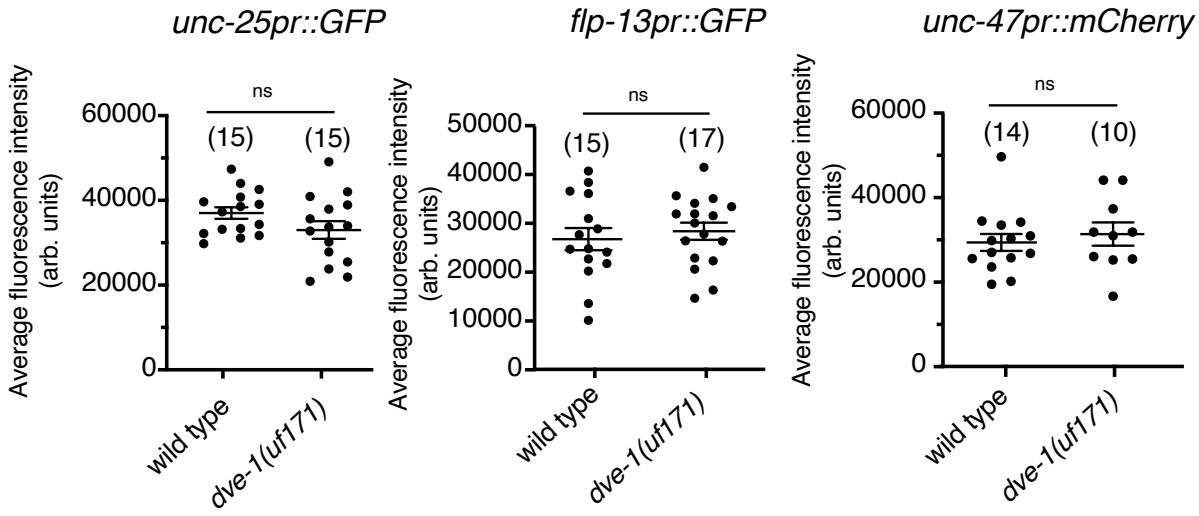
unc-25pr::GFP
flp-13pr::GFP
unc-47pr::mCherry
Average fluorescence intensity (arb. units)
ns
(15)
(15)
(15)
(17)
(14)
(10)
60000
40000
20000
0
50000
30000
10000
wild type
dve-1(uf171)

Supplemental Figure 6.2. Mutation of *dve-1* does not alter GABAergic neuronal identity

(A) Representative image of wild type (right) and *dve-1(uf171)* mutant (left) animals expressing *punc-25::GFP* to label DD neurons at the L1 stage. * indicates cell body.

(B) Average fluorescence intensity of *unc-47pr::mCherry,* and *unc-25pr::GFP, flp-13pr::GFP* reporters in DD1, DD2, and DD3 neuron cell bodies of L1 stage wild type and *dve-1(uf171)* mutants. Each dot represents the average of three cell bodies in a single animal. Bars indicate mean ± SEM. n: not significant, two-tailed students t-test.

a

DVE-1 binding motifs

p-value

8.9e-23

5.5e-19

2.9e-33

2.1e-16

b

Supplemental Figure 7.1. Enrichment analysis of putative DVE-1 targets reveals potential pathways governing synapse elimination

(A) *de novo* motif discovery analysis of 968 DVE-1 binding peaks identifies 4 DVE-1 binding motifs.

(B) Wormcat analysis for enriched categories of putative DVE-1 targets identified from ChIP-seq dataset. Size of circles indicates the number of genes and color indicates the significance value for over-representation in each Wormcat category.

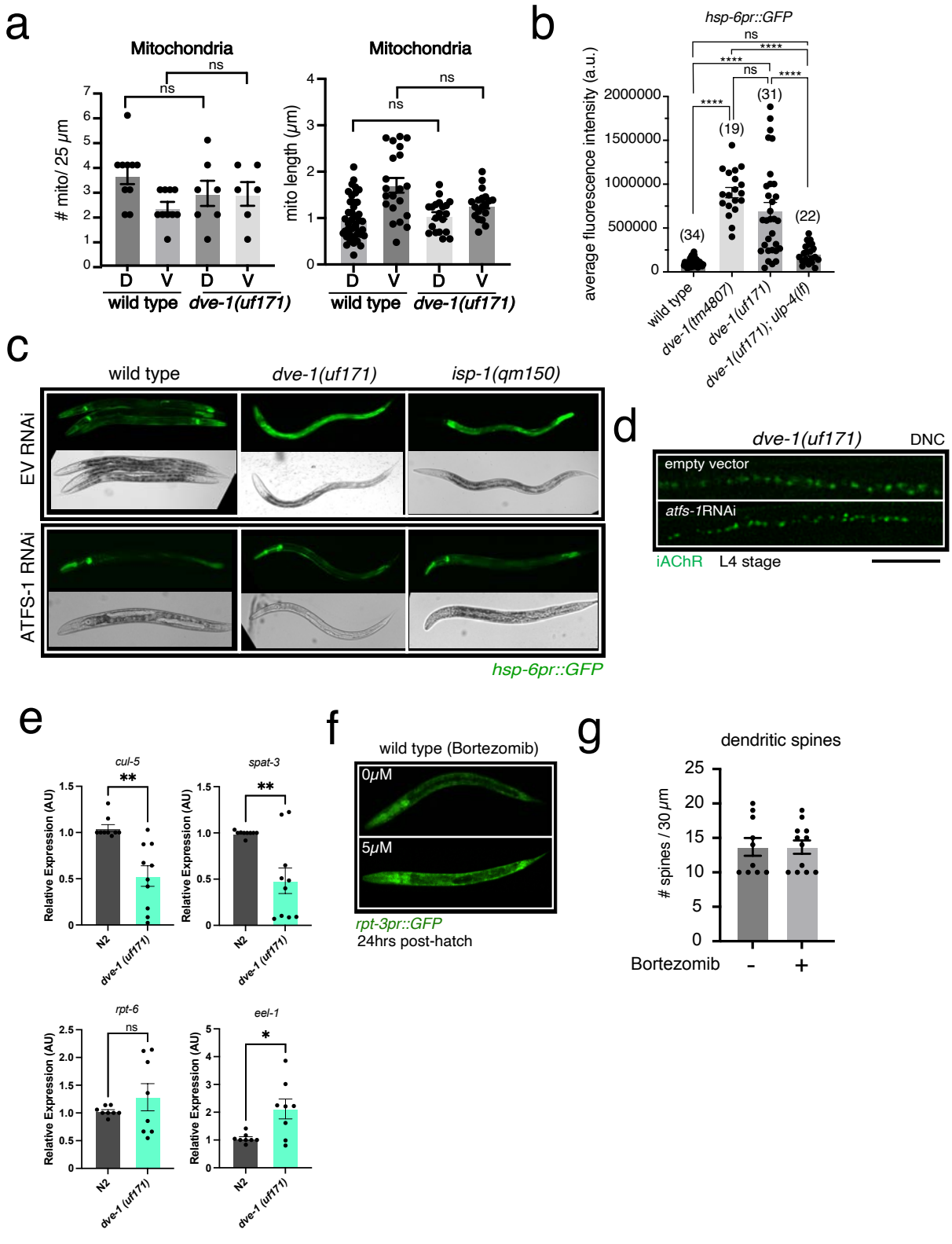
a
Mitochondria
mito/ 25 µm
ns
D V D V
wild type dve-1(uf171)
Mitochondria
mito length (µm)
b
hsp-6pr::GFP
average fluorescence intensity (a.u.)
(34)
(19)
(31)
(22)
wild type
dve-1(tm4807)
dve-1(uf171)
dve-1(uf171); ulp-4(lf)
c
wild type
dve-1(uf171)
isp-1(qm150)
EV RNAi
ATFS-1 RNAi
hsp-6pr::GFP
d
dve-1(uf171)
DNC
empty vector
atfs-1RNAi
iAChR
L4 stage
e
cul-5
spat-3
rpt-6
eel-1
Relative Expression (AU)
N2
dve-1 (uf171)
f
wild type (Bortezomib)
0µM
5µM
rpt-3pr::GFP
24hrs post-hatch
g
dendritic spines
spines / 30 µm
Bortezomib

Supplemental Figure 7.2. Removal of iAChRs in GABA motor neurons is not affected by activation or inhibition of the mtUPR

(A) Left, scatterplot of mitochondrial density (number of mitochondria/25 μm) in dorsal (D) and ventral (V) processes of DD neurons of L4 stage wild type and *dve-1(uf171)* mutants. Each point represents a single animal. wild type, n=10; *dve-1(uf171)*, n=6. Right, average length of mitochondria in dorsal and ventral processes of DD neurons of L4 stage wild type and *dve-1(uf171)* mutants. Each dot represents a single mitochondrion. wild type, n=10; *dve-1(uf171)*, n=6. Bars indicate mean ± SEM. ns: not significant, two-way ANOVA with Tukey's multiple comparisons test.

(B) Average intestinal fluorescence intensity measures for wild type, *dve-1(tm4807)*, *dve-1(uf171)* and *dve-1(uf171);ulp-4(lf)* animals expressing *hsp-6pr::GFP*. Bars represent mean ± SEM. One way ANOVA with Tukey's multiple comparisons test. **p <0.01, ****p< 0.0001.

(C) Fluorescent images of transgenic worms expressing the mtUPR reporter *hsp-6pr::*GFP and treated with either empty vector (top) or RNAi targeting *atfs-1* (bottom). *dve-1(uf171)* mutants show increased expression of *hsp-6pr::*GFP under basal conditions compared with control animals and this is reversed by RNAi targeting *atfs-1*. *isp-1* mutants also have elevated mtUPR and are included as a control.

(D) Fluorescent confocal images of iAChR clusters in dorsal nerve cord (DNC) of DD neurons of L4 stage *dve-1(uf171)* mutants treated with either empty vector or RNAi targeting *atfs-1*. *atfs-1* RNAi reverses mtUPR activation in *dve-1* mutants but does not normalize synapse elimination. Scale bar, 5 μm.

(E) Quantitative RT-PCR analysis of predicted DVE-1 targets. Mutation of *dve-1* significantly alters *cul-5*, *spat-3*, and *eel-1* expression, normalized to *act-1* levels. Each point indicates an independent technical replicate. Bars represent mean ± SEM. ***p*<0.001, * *p*<0.05, Welch's t test.

(F) Fluorescent images of transgenic worms expressing the *rpt-3pr::GFP* reporter with or without treatment with the proteasome inhibitor Bortezomib (5 μM).

(G) Quantification of the average number of dendritic spines in L4 stage wild type animals under either control conditions (n=10) or following Bortezomib treatment (n=12). Each dot represents a single animal. Bars represent mean ± SEM.

Supplementary Table 1: DVE-1 ChIP-seq targets

Ubiquitin-Proteasome System DVE-1 ChIP-seq targets			
C. elegans	***H. sapiens***	**Gene Description**	**Enrichment tool**
		Proteasome subunit/composition	
pas-5	PSMA5	proteasome subunit alpha 5 (20S proteasome)	WormCat, WikiPathways (wormenrichr)
rpt-5	PSMC3	proteasome 26S subunit ATPase 3 (26S proteasome)	WormCat, WikiPathways (wormenrichr)
rpt-6	PSMC5	proteasome 26S subunit ATPase 5 (26S proteasome)	WormCat, WikiPathways (wormenrichr)
		Ubiquitin	
ubq-1	UBC	Ubiquitin, polyubiquitin locus	WormCat, WikiPathways (wormenrichr)
		E2 Enyzme	
ubc-2/let-70	UBE2D1/UBE2 D2/UBE2D3	E2 ubiquitin conjugating enzyme	WormCat, WikiPathways (wormenrichr)
		E3 Enzyme HECT-Domain	
wwp-1	ITCH	HECT-domain ubiquitin E3 ligase	WormCat
eel-1	HUWE1	HECT-domain ubiquitin E3 ligase	WormCat
		E3 Enzyme RING-finger complex	
cul-5	CUL5	RING finger complexe cullin 5	WormCat
rfp-1	RNF20	ring finger protein 20	WormCat
C11H1.3	MGRN1	mahogunin ring finger 1	WormCat
rnf-113	RNF113A	ring finger protein 113A	WormCat
spat-3	RING1/RING2	ring finger protein 1/2	WormCat
		DUB Enzymes	
usp-48	USP48	Ubiquitin-Specific Protease 48	WormCat
usp-14	USP14	Ubiquitin-Specific Protease 14	WormCat
otub-1	OTUB1/2	otubain-1/2	WormCat
H34C03.2	USP11	Ubiquitin Specific Peptidase 11	WormCat
T22F3.2	USP17L1	Ubiquitin Specific Peptidase 17 Like Family Member 1	WormCat
otub-2	OTUD7A	OTU Deubiquitinase 7A	WormCat
		UPS associated	
C46F11.6	UBL3	Ubiquitin-like 3	WormCat
wdr-23	DCAF11/WRD23	DDB1 and CUL4 associated factor 11	WormCat
ubql-1	UBQLN4	ubiquilin 4	WormCat
atg-7	ATG7	autophagy related	WormCat
ppm-2	PPM1A	protein phosphatase, Mg2+/Mn2+ dependent 1A	WormCat
K02A6.3		F-box domain	WormCat
spsb-1	SPSB1	a Spry domain-containing socs box protein	WormCat
cpi-2	CST3/6	cystatin C/ cystatin E/M	WormCat
try-6	TMPRSS13	transmembrane serine protease 13	WormCat
spcs-3	SPCS3	signal peptidase complex subunit 3	WormCat